Article

Investigation into the Aerodynamic Performance of a Vertical Axis Wind Turbine with Endplate Design

Shern-Khai Ung [1], Wen-Tong Chong [2], Shabudin Mat [3], Jo-Han Ng [1], Yin-Hui Kok [1] and Kok-Hoe Wong [1,*]

1 Department of Mechanical Engineering, Faculty of Engineering and Physical Sciences, University of Southampton Malaysia, Iskandar Puteri 79200, Malaysia
2 Department of Mechanical Engineering, Faculty of Engineering, Universiti Malaya, Kuala Lumpur 50603, Malaysia
3 Institute for Vehicle Systems and Engineering (IVeSE), Universiti Teknologi Malaysia, Skudai 81310, Malaysia
* Correspondence: k.h.wong@soton.ac.uk; Tel.: +60-165363421

Abstract: For the past decade, research on vertical axis wind turbines (VAWTs) has garnered immense interest due to their omnidirectional characteristic, especially the lift-type VAWT. The H-rotor Darrieus VAWT operates based on the lift generated by aerofoil blades and typically possesses higher efficiency than the drag-type Savonius VAWT. However, the open-ended blades generate tip loss effects that reduce the power output. Wingtip devices such as winglets and endplates are commonly used in aerofoil design to increase performance by reducing tip losses. In this study, a CFD simulation is conducted using the sliding mesh method and the *k-ω SST* turbulence model on a two-bladed NACA0018 VAWT. The aerodynamic performance of a VAWT with offset, symmetric V, asymmetric and triangular endplates are presented and compared against the baseline turbine. The simulation was first validated with the wind tunnel experimental data published in the literature. The simulation showed that the endplates reduced the swirling vortex and improved the pressure distribution along the blade span, especially at the blade tip. The relationship between TSR regimes and the tip loss effect is also reported in the paper. Increasing VAWT performance by using endplates to minimise tip loss is a simple yet effective solution. However, the improvement of the power coefficient is not remarkable as the power degradation only involves a small section of the blades.

Keywords: endplate; wingtip device; blade tip losses; Darrieus VAWT; CFD

1. Introduction

As global warming and environmental issues continue to be aggravated, people have begun to shift their focus from non-renewable resources to sustainable and renewable resources for power generation. Wind energy has gained traction and become a prominent source of renewable energy. According to the Global Wind Energy Council (GWEC) [1], 93.6 GW of wind capacity was installed in 2021 globally, leading to a total wind capacity of 837 GW, which is a 12.4% increase from 2020. Wind turbines (WTs) of scales up to megawatts are widely deployed in onshore and offshore regions to capture wind energy. There are two common types of wind turbines—horizontal axis wind turbines (HAWTs) and vertical axis wind turbines (VAWTs), in which their rotor rotates on a different axis, as the name suggests. Currently, HAWTs make up most of the WTs in the market due to their higher efficiency compared to VAWTs [2–5]. However, a large megawatt-scale HAWT has its downsides and limitations, such as an increase in cost and weight with blade length [3,6]. Meanwhile, the omnidirectional characteristics and simplified machine design of VAWTs have attracted researchers' interest, leading to rigorous research and development in the past few years [3,5].

VAWTs are further categorised into the lift type (Darrieus) and the drag type (Savonius), corresponding to their operating principle. The former has higher efficiency and is driven by the pressure difference across the aerofoil blade, while the latter has a better

self-start ability and generates torque from the drag force acting on the concave blades [7]. It is crucial to understand the complex flow characteristics of VAWTs, which are very different from HAWTs. The VAWT suffers from tip losses at both ends of the blade, blade–wake interaction in the downwind region, and dynamic stalls caused by the continuous variation in the angle of attack throughout a revolution [8–10]. According to the study of a three-bladed VAWT model performed by Howell et al. [11], the interaction with wake can affect the pressure distribution on the blade. Vortex strength is found to be correlated with the lift generated by the blades, where the tip vortex generated is the strongest right after the blade has attained maximum lift. The tip vortex becomes weaker in the downstream region, and the overall power output of the VAWT is reduced compared to an ideal 2D case.

To weaken these blade tip losses, wingtip devices such as endplates, elliptical terminations, and winglets are commonly utilised in the aerospace and automotive sector to improve aerodynamic performance. These wingtip devices reduce spanwise flow due to the pressure difference between both sides of an aerofoil and improve the aerodynamic characteristic of the wing or blade [9,12–14]. For instance, Jung et al. [13] numerically investigated the effect of an endplate on a wing-in-ground (WIG) craft's wingtip over the free surface. With a NACA4406 profile blade in an aspect ratio of 2, their simulation revealed that the endplate improves the pressure distribution on both sides of the wing, especially on the pressure side. The blockage effect introduced by the endplate enhances the air cushion effect on the wing, leading to a 14% and 124% improvement in the power coefficient (C_P) near the leading edge and the trailing edge, respectively. An increase of up to 46% in the lift-to-drag ratio is also observed when the wing is close to the free surface; however, these improvements become negligible as the wing is further away from the ground due to a weaker WIG effect. Although a larger vortex is generated at the endplate tip due to flow separation, the lateral motion of the tip vortex helps to reduce the induced drag.

Wingtip devices are also implemented in HAWTs to improve aerodynamic efficiency and power output. Johansen and Sørensen [15] studied the effect of winglet parameters on a HAWT's performance. All configurations with winglets lead to power enhancements ranging from 0.98% to 2.77%. Twist angles have negligible effects on power and thrust, while a smaller curvature radius leads to larger power increments. With a 30° sweep angle imposed on the winglet, the performance improvement is reduced compared to no sweep angle.

However, the beneficial effect of wingtip devices is highly dependent on the wing parameters and use case scenario. For example, the effect of an endplate on a VAWT blade that rotates around its vertical axis is different from its application in an airplane or a car, where the oncoming wind direction is more consistent. Thus, the existing research data from other fields cannot represent a VAWT's characteristics. Extensive research is required to find the optimised wingtip device design for VAWTs, as a wrongly designed wingtip device may adversely affect the VAWT's performance [16].

Laín et al. [4] studied the effects of winglets on a straight-bladed Darrieus water turbine and found that both symmetric and asymmetric winglets can improve turbine performance. The symmetric winglet particularly brings 20% power enhancement, in which the improvement mainly occurs at the maxima that coincides with the location where maximum lift is obtained. However, the power augmentation leads to a larger thrust acting on the blades and, thus, requires extra attention to the structural strength when winglets are employed. Besides that, the long trailing vortex generated in the bare blade is weakened with the asymmetric winglet, while the symmetric blade eliminates the trailing vortex. The detachment of vorticity still occurs with winglets but is delayed compared to the bare blade.

Syawitri et al. [14] reviewed a range of passive flow control devices (PFCDs) to enhance the lift-type VAWT's performance via minimising flow separation and reducing dynamic stalls without external power input. Winglets weaken the tip vortex by preventing flow mixing between the pressure and suction sides at the blade tip. This can lead to a 10–19% improvement in the low tip speed ratio (TSR) regime and a 6.7–10.5% improvement in

the medium regime. However, the C_P improvement diminished as the regime of TSRs increased. Other PFCDs, such as inward dimple and gurney flap, can also enhance the C_P of VAWTs, but every device performs differently across different TSR regimes. For instance, a 2D simulation conducted by Mousavi et al. [17] on a Darrieus VAWT with NACA0021 aerofoil found that the gurney flap installed on either the suction or pressure side of the blade results in power enhancement in the low TSR range (i.e., 0.6 to 1.6). The reverse was observed at TSRs of 1.8 to 3. The study also discovered that a gurney flap installed at an angle towards the blade surface, in general, offers better performance over the standard configuration.

The effect of the curvature radius of a winglet attached to a three-bladed VAWT was studied by Malla et al. [2]. They found that the aerodynamic performance increases as the curvature radius decreases, and this result coincides with the findings in [15] on HAWTs. The lift coefficient showed an increase in the upstream region, while the opposite results were observed in the downstream region. The largest pressure difference on the blade happened at a 90° azimuthal angle, and the addition of winglets led to lower minimum pressure on the suction side and a larger area of maximum pressure on the pressure side.

Besides winglets, endplates, which are sometimes referred to as bulkheads in the literature [16,18], are also implemented in both lift- and drag-type VAWTs. Premkumar et al. [19] set up an experiment to test a helical Savonius drag-type VAWT with and without a circular endplate. The presence of the endplate lowered the torque coefficient and raised the power coefficient of the VAWT across wind speeds of 3–6 m/s due to a higher TSR achieved. With a conventional Savonius VAWT, the 3D CFD conducted by Kassab et al. [20] showed that a larger pressure difference is achieved when a circular endplate is installed, as it acts as a physical barrier to block spanwise flow. The endplate also smoothens flow through the turbine but generates more vortices at the blade tip. At the optimum TSR of 0.8, the average lift and drag coefficients were elevated by 400% and 180%, respectively, while the C_P saw a 42.5% improvement over the bare VAWT.

Amato et al. [16] analysed and compared the effect of the endplate, elliptic tip, and winglets on a lift-type VAWT. All configurations managed to improve C_P over the baseline rotor; however, the winglet with a 90° cant angle performed the best over TSRs 2.65 to 3.7, with an 11.85% increment at 620 rpm. The 50% longer version of the same winglet showed less improvement due to the decrease in the pressure torque on the profile.

Miao et al. [12] studied the effect of 20 blade tip device designs, including winglets and endplates, on the aerodynamic performance of an H-rotor Darrieus VAWT. With the same aspect ratio and sweep area, they found that the flat endplate with an offset of 0.18c from the blade profile improves C_P, but the improvement degrades at higher TSR due to larger drag. Reduction of drag can be achieved by implementing a streamlined shape on the top surface, and the study showed that only the streamline-shaped endplate and a novel Winglet-H could improve the C_P at TSRs 1.85, 2.29, and 2.52. This study revealed that the blade tip devices predominantly affect the blade tip region without pronounced effects on the pattern of wake propagation of the VAWT.

Daróczy et al. [21] investigated the effect of different parameters of a winglet and compared it with the baseline and endplate cases. At TSR 2.6, all configurations barely improved C_P at the region 0.1 m away from the blade tip. Overall, the endplate slightly improved the C_P by 0.65%, while all six winglet configurations tested in this study not only failed to improve the turbine performance but were subpar to the baseline VAWT. This further emphasises the importance of implementing a well-optimised winglet or wingtip device for a VAWT.

Jiang et al. [18] performed a numerical simulation on a single-bladed rotor with an aspect ratio of 15. They observed the tip loss effect until 3c from the blade tip, where the torque coefficient remained negative throughout the cycle at 0.05c. The implementation of the endplate smoothens the flow at the blade tip and improves the work done by the blades. A larger endplate shows a greater enhancement in blade work. However, it induces more drag, which offsets a large portion of the gains achieved. Thus, the optimal size of the

endplate is found to be 0.35*c*. However, this configuration deteriorates the performance at low TSRs. The same observation is reported in [14], where flow control devices performed differently across all TSR regimes.

Gosselin et al. [9] performed simulations on a single-bladed NACA0015 turbine with aspect ratios (ARs) 7 and 15, where the larger AR blade attained a better C_P of 62.5%. This indicates that a short blade suffers greater tip loss effects due to a large portion of the blade being influenced by the tip effects. Therefore, low AR blades may benefit more from wingtip devices. The addition of endplates reduces the blade tip effect and produces uniform pressure distribution across the length of the blade. However, a larger endplate induces more drag and ultimately exceeds the power enhancement on the VAWT.

Nathan and Thanigaiarasu [22] investigated the effect of aerofoil-shaped, rectangular and full circular endplates on the aerodynamic performance of a three-bladed VAWT. The aerofoil-shaped and rectangular endplate managed to elevate the C_P by up to 3%. However, the extra mass introduced by the full circular endplate, which covers the entire rotor, failed to bring positive results. The full circular endplate also induced the largest load on the blades at 80% to 90% span, where 90% span is closer to the blade tip.

The results presented by Mishra et al. [23] through experiments and simulations showed that endplates levitated the C_P of a three-bladed VAWT with a NACA0018 blade profile. Endplates also increased the rotational speed of the turbine at the same wind velocity compared to the baseline turbine. Opposite results were observed with winglets due to the larger overall drag induced. To provide a clearer view of the literature review, the wingtip devices discussed above are summarised in Table 1 below.

Table 1. A summary of wingtip devices from the literature review.

Author	Wingtip Device	Parameter	Application	Main Finding
Jung et al. [13]	Endplate	Distance from the free surface	WIG craft	14% and 124% improvement in C_P at the leading edge and trailing edge, respectively. Improvement degrades as the distance from the free surface increases.
Johansen and Sørensen [15]	Winglet	Winglet height, sweep angle, curvature radius, twist angle	HAWT	Power improved by 0.98% to 2.77%. A smaller curvature radius generates larger power improvements.
Laín et al. [4]	Winglet	Symmetric and asymmetric winglet	Darrieus water turbine	Symmetric winglet brought a larger improvement at 20%.
Syawitri et al. [14]	Winglet and others	-	Lift-type VAWT	10–19% power improvement in the low TSR regime and 6.7–10.5% at the medium regime.
Mousavi et al. [17]	Gurney Flap	Placement of flap and angle	Two-bladed lift-type VAWT	Gurney flap enhances C_P at low TSRs. Angled gurney flap provides superior performance over standard gurney flap configuration.
Malla et al. [2]	Winglet	Curvature radius	Lift-type VAWT	Aerodynamic performance increases as the curvature radius decreases.
Premkumar et al. [19]	Endplate	Presence of endplate	Savonius drag-type helical VAWT	Endplate lowers the torque coefficient and raises the power coefficient.
Kassab et al. [20]	Endplate	Presence of endplate	Savonius drag-type VAWT	The average lift and drag coefficients were elevated by 400% and 180%, respectively, while the C_P saw a 42.5% improvement over the bare VAWT at TSR 0.8.
Amato et al. [16]	Winglet, elliptical termination and endplate	Winglet—cant angle and winglet length	Single-bladed lift-type VAWT	Winglet with 90° cant angle achieved 11.85% increment at 620 rpm.
Miao et al. [12]	Winglet and endplate	Wingtip device designs	H-rotor Darrieus VAWT	Improvements from the endplate degrade as TSR increases. Only the streamlined-shaped endplate and a novel Winglet-H can improve C_P over a larger range of TSRs.
Daróczy et al. [21]	Winglet and endplate	Cant angle and sweep angle	Three-bladed lift-type VAWT	All 6 winglet configurations reduced the power output compared to the baseline turbine. Endplate improved power output by 0.65%.
Jiang et al. [18]	Endplate	Endplate offset	Single-bladed lift-type VAWT	The optimal size of endplate is 0.35*c*.
Gosselin et al. [9]	Endplate	Aspect ratio and endplate shape	Single-bladed lift-type VAWT	Lower AR blades suffer larger tip losses. Endplates reduce the blade tip effect, but overly sized endplates decrease the turbine performance.
Nathan and Thanigaiarasu [22]	Endplate	Endplate Shape	Three-bladed lift-type VAWT	The aerofoil-shaped and rectangular endplates elevated the C_P by up to 3%, while the full circular endplate, which covers the entire rotor, showed negative results.
Mishra et al. [23]	Endplate	Endplate offset	Three-bladed lift-type VAWT	Endplates levitated the C_P and RPM of the turbine.

After reviewing various literature, wingtip devices exhibit the potential to elevate the performance of a VAWT. However, there is limited research on the variation of endplate geometry for the aerodynamic performance of a Darrieus VAWT compared to winglet geometry. Endplates with simple offset from the blade profile have been employed in previous papers, while other possible geometries are rarely proposed. Therefore, this paper aims to explore the effect of different endplate geometries on the aerodynamic performance of a Darrieus VAWT, vortex generation, pressure distribution on the turbine blades and the drag induced. The research findings can provide insight and comparison on the implications of endplate geometry on a VAWT, especially around the blade tip region. In the next section, details of the wind turbine model, simulation setup and validation are presented. Section 3 presents the results and a discussion of the findings obtained from the simulation, and a comprehensive conclusion is deduced in Section 4.

2. Methodology

2.1. Aerodynamics of the H-Rotor Darrieus VAWT

An H-rotor Darrieus VAWT consists of two straight blades with an aerofoil-shaped cross-section. As the name suggests, the rotor rotates about the vertical axis, and thus, the flow characteristics are different from those of HAWTs. Unlike HAWTs, the power output of a VAWT varies with the azimuthal angle. The blade–wake interaction in the downstream region (i.e., $180° \leq \theta \leq 360°$) leads to a much lower power output compared to the upstream region (i.e., $0° \leq \theta \leq 180°$), which receives undisturbed wind. To quantify turbine performance, the dimensionless coefficient of torque (C_T) and coefficient of power (C_P) is derived as shown below:

$$C_T = \frac{T}{\frac{1}{2}\rho A R U_\infty^2} \tag{1}$$

where T is the torque generated, ρ is the air density, A is the swept area, R is the rotor radius and U_∞ is the free stream velocity.

$$C_P = \frac{P}{\frac{1}{2}\rho A U_\infty^3} \tag{2}$$

where P is the power generated. According to the Betz limit, C_P = 0.593 is the upper limit tht a wind turbine can achieve.

Another crucial non-dimensional parameter of a wind turbine is the tip speed ratio (TSR). It is the ratio of the velocity at the blade tip to the incoming wind velocity, and it is denoted as λ. The TSR is defined as:

$$\lambda = \frac{R\omega}{U_\infty} \tag{3}$$

where ω is the angular velocity of the rotor. Since power is equivalent to the product of torque and angular velocity, Equation (2) can be simplified into:

$$C_p = \lambda \cdot C_t \tag{4}$$

As aforementioned, VAWTs suffer from tip losses at the blade tip, which can only be captured through 3D simulation [24]. The studies done by Howell et al. [11], Lam et al. [8], and Gosselin et al. [9] show that 2D simulation consistently overestimates C_P while the 3D case predicts C_P values closer to the experimental data. This is due to the 2D model resembling a blade with infinite length; the simulation cannot capture the flow in the span-wise direction and vortical motion at the blade tip. Therefore, a 3D numerical simulation is adopted in this study to properly capture the tip loss effects in VAWTs.

2.2. Rotor Geometry

In this study, a straight-bladed H-rotor Darrieus VAWT is modelled, as illustrated in Figure 1, based on the rotor specifications adopted in the wind tunnel experiment conducted by Watanabe et al. [25]. The VAWT model has a rotor height (*H*) of 700 mm and a diameter (*D*) of 700 mm. It comprises two blades with a chord length (*c*) of 150 mm and no pitch angle. Although omitting the shaft and supporting structure can lead to the overestimation of results [26,27], the current study aims to compare turbine performance based on endplate geometry. Therefore, the two NACA0018 profile blades are modelled in the rotor domain without the centre shaft and spoke to simplify the mesh. As shown in Figure 1, six cut sections with a width of 5 mm each are made on Blade 1 at heights 0.015625*H*, 0.03125*H*, 0.0625*H*, 0.125*H*, 0.25*H* and 0.5*H* from the blade tip (i.e., the top end) to extract the C_P values at these locations and observe the blade tip loss effect.
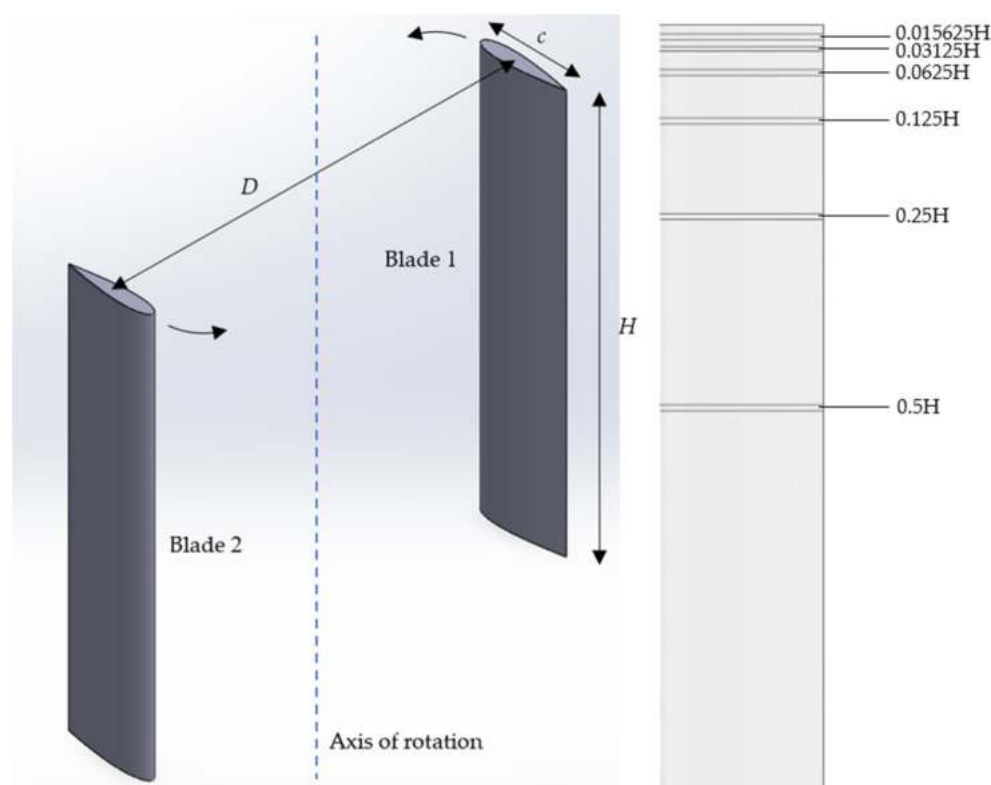

Figure 1. NACA0018 straight-bladed VAWT and cut sections adopted in the current simulation.

2.3. Endplate Geometry

To compare and study the effect of endplates on blade tip losses, the endplates are modelled on both ends of each blade. All endplate configurations have a flat surface with a thickness of 0.03*c*, which is also adopted in the literature [12,18]. The aspect ratio of a VAWT blade is the ratio of the blade height to the chord length, and this parameter can affect the power output of a VAWT [9,12,21]. To maintain the aspect ratio for a fair comparison with the baseline rotor, the overall height of the blade, including the endplates, is kept the same as the baseline rotor height. Four different endplates—offset, symmetric V, asymmetric, and triangular endplates—are investigated in this study, as depicted in Figure 2. The offset endplate is modelled with an offset of 0.35*c* from the blade profile, which is claimed to be optimal according to [18], while the symmetric V endplate has a pointed V-shape design. The asymmetric endplate has a larger area allocated, facing the inside of the rotor, in which the flow is more complex [4], whereas the triangular endplate has a similar profile as the symmetric V endplate but with a flat trailing edge. All sharp edges on the endplates are eliminated by applying a 5 mm radius fillet at the trailing edge and a 10 mm radius at the pointed leading edge.
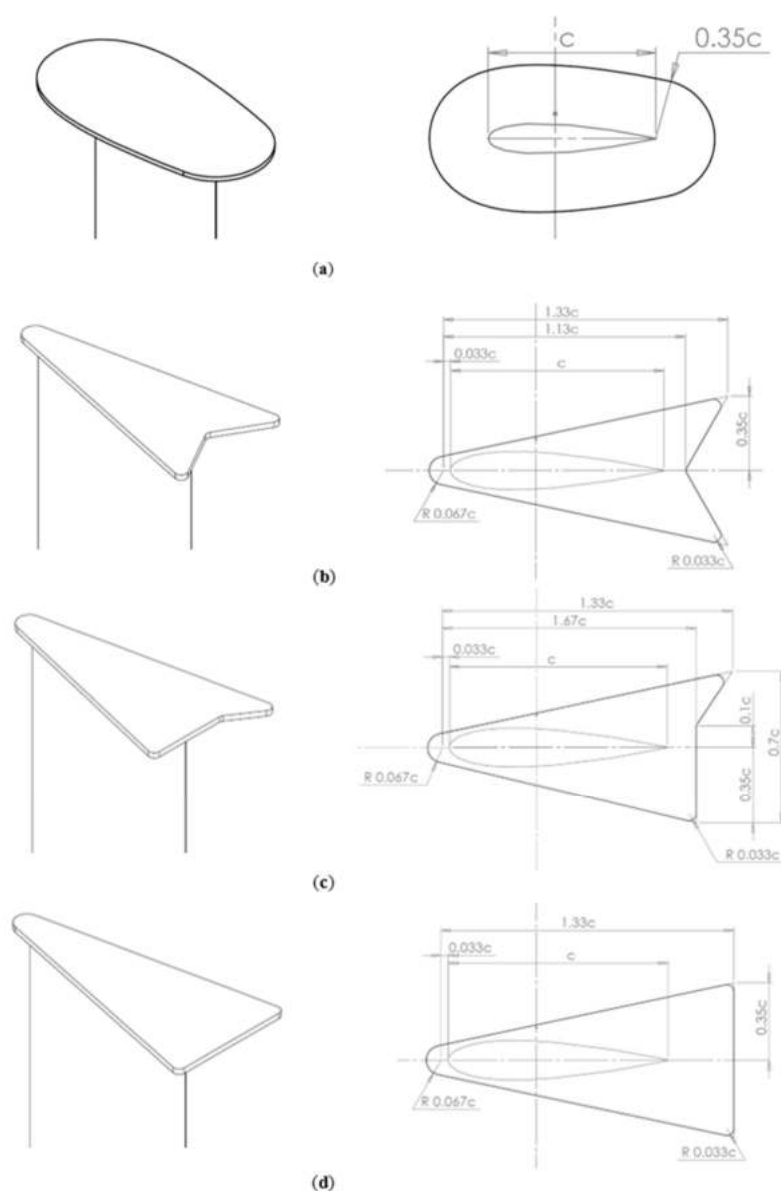
Figure 2. Endplate geometries: (**a**) 0.35*c* offset endplate; (**b**) symmetric V endplate; (**c**) asymmetric endplate; (**d**) triangular endplate.

2.4. Sub-Domain of CFD and Boundary Conditions

The CFD simulation model consists of a cylindrical VAWT rotor and a rectangular tunnel domain. The tunnel domain is modelled with a dimension of 16*D* (length) × 10*D* (width) × 10*D* (height), and the surfaces on the side are set symmetrically. The outlet gauge pressure is set at 0 Pa, and the turbulence intensity and length scale are set to 0.5% and 10.5 mm, respectively. In order to replicate the results obtained from the wind tunnel experiment, the incoming wind is set to be uniform and has a velocity of 6 m/s, as reported by Watanabe et al. [25]. Meanwhile, the rotor domain, located at 6*D* from the inlet, is modelled with a cylindrical enclosure with an offset of 0.1 m on the side and 0.25 m on the top and bottom of the blades/endplates. This is to ensure sufficient space for a gradual transition of mesh between the blade and the boundaries as well as to maintain a higher mesh quality during the meshing stage. The rotor domain is set to rotate at $\omega = 17.14$ rad/s and $\omega = 34.29$ rad/s to achieve TSRs 1 and 2, respectively, for this study. The blockage factor, which is the ratio of the rotor frontal area to the tunnel cross-sectional area, in the simulation is only 1% for the baseline VAWT, which falls within the acceptable range of less than 6–7.5% for numerical simulations [8]. The three boundaries between the rotor and

tunnel domain were regarded as interfaces to allow cell zones to connect from one mesh to another using the sliding mesh method. Both sub-domains and their respective boundary conditions applied are shown in Figure 3.
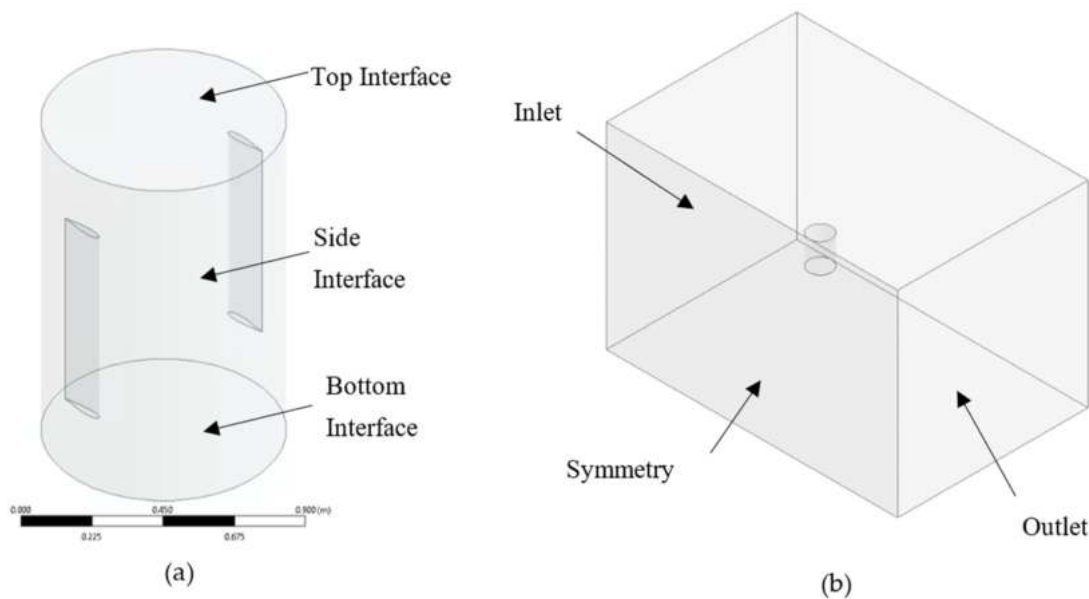

Figure 3. Sub-domains in current CFD simulation. (**a**) Rotor domain; (**b**) tunnel domain.

2.5. Solver Settings

A commercially available simulation software that is based on the finite volume method, Ansys Fluent, is adopted in this study to carry out all the numerical simulations on a VAWT. The pressure-based solver includes relevant variables, such as momentum and pressure, to be taken as the primary variables [28]. The absolute velocity formulation is adopted, while time dependency is set to transient. The current simulation utilises the k-ω SST (shear stress transport) turbulence model [29], which is widely adopted for the simulation of VAWTs [2,9,16,18,23,30,31]. This model combines the standard k-ω model at near-wall regions and the k-ε model at regions beyond the boundary layer [28]. In Gosselin et al.'s [9] investigation, they concluded that the k-ω SST model offers a better dynamic stall representation while simulating a relatively lower cost compared to transition SST. Under the reference value section, the solver is set to compute from the inlet, with the rotor domain being set as the reference zone. This happens while the pressure–velocity coupling runs with the default Semi-Implicit Method for Pressure Linked Equation (SIMPLE) scheme in the solution methods section. The solution gradient was set to least square cell-based with standard pressure. The momentum, turbulent kinetic energy, and the specific dissipation rate were set to a second-order upwind scheme, and the transient formulation was set to a second-order implicit method to obtain results with better accuracy. Default values were maintained for the variables in the under-relaxation factors as well as the fluid settings, where the air density and viscosity are kept at 1.225 kg/m^3 and 1.7894×10^{-5} kg/ms, respectively. The absolute convergence criteria for all residuals are set to 1×10^{-5} to attain species balance [28]. The average C_T achieved by the turbine blades over one revolution is extracted from the simulation and converted into C_P using Equation (4). The simulation continues until the percentage difference of C_P between two consecutive revolutions, calculated using Equation (5), as shown below, is less than 1%.

$$\frac{C_{P,ave(n+1)} - C_{P,ave(n)}}{C_{P,ave(n)}} \times 100\% < 1\% \tag{5}$$

As the rotor domain rotates around its axis during the simulation, a suitable timestep is crucial to ensure the stability of a simulation and achieve convergence in the results. The

current simulation adopted a 1° rotation per timestep (equivalent to 1.01811×10^{-3} s per time step and 5.0905×10^{-4} s per time step for TSRs 1 and 2, respectively), which is widely used in VAWT simulations to achieve a balance in result accuracy and simulation time [30]. At each timestep, the simulation will run for a maximum of 20 iterations before proceeding to the next timestep. To analyse the aerodynamic characteristic at different azimuthal angles, the data is saved every 30 timesteps once the results have reached convergence. Before starting the simulation, the solution is initialised with the standard initialisation, which computes from the inlet.

2.6. Model Validation and Mesh Independent Test

All configurations of the rotor are modelled using the SolidWorks software before being imported into the Design Modeller to create the cylindrical rotor domain. For capturing the flow in the rotor domain, the mesh is made to be very dense, with fine elements near the blade surfaces. Face meshing is applied to the blade span surface to obtain a structured mesh. Meanwhile, an inflation layer is applied in the near-wall region to further refine the mesh and capture the boundary layer gradients. The first layer thickness is set to 0.1 mm, with a maximum of 15 layers and a thickness growth rate of 1.2, to achieve a y^+ value of around 1. The y^+ value, as defined below, is a dimensionless parameter that can be used to classify types of boundary layers.

$$y^+ = \frac{u \cdot y}{v} \tag{6}$$

where u is the shear velocity at the nearest wall, y is the absolute cell distance from the nearest wall and v is the fluid local kinematic viscosity. When the y^+ value is less than 5, it is considered a laminar sub-layer [30,32].

In the meantime, the tunnel domain is modelled and meshed separately. The mesh size at the tunnel side interface is set to 10 mm to match the sizing on the rotor interface for a better connection between the two meshes. The generated rotor and tunnel mesh are appended into Ansys Fluent, with the rotor domain being situated within the tunnel domain. There is no overlapping of meshes where both meshes are connected through their respective interfaces.

The refinement of mesh is conducted on the blade surface to ensure accurate results are obtained, as shown in Figure 4, where 85% of the cells are found in the rotor domain in all cases.
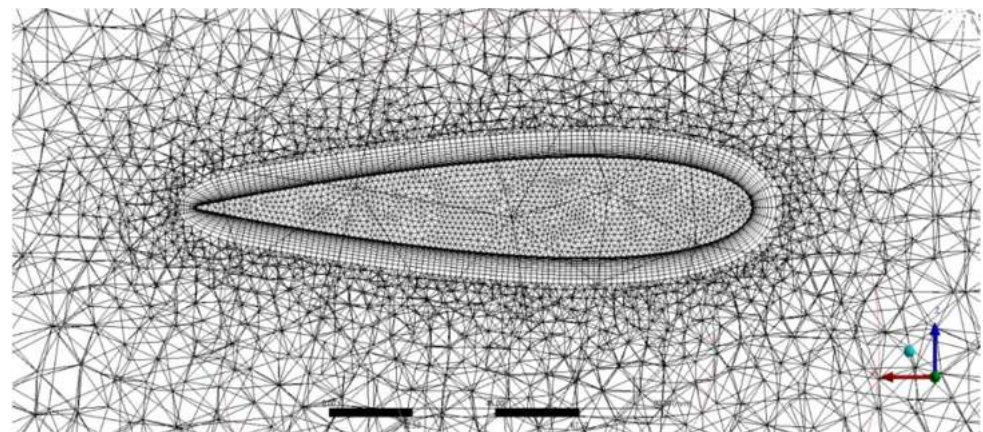

Figure 4. Sectional view of mesh around the blade surface in the rotor domain.

The baseline VAWT model is first validated with the experimental data by Watanabe et al. [25], who studied the same VAWT configuration as the current VAWT model. The VAWT model is simulated over a range of TSRs, from 0.5 to 2.5, with an inlet velocity of 6 m/s, and the result is compared with the experimental data, as illustrated in

Figure 5. The current model replicates the overall trend of the experimental data well, with a slight underestimation of C_P at TSRs 1 to 2. Discrepancies are observed at TSRs 0.75 and 2.5, with a percentage error of around 9–10%. Nevertheless, the VAWT model can produce satisfactory results over the TSR range; hence, the simulation is continued with the mesh independence test.
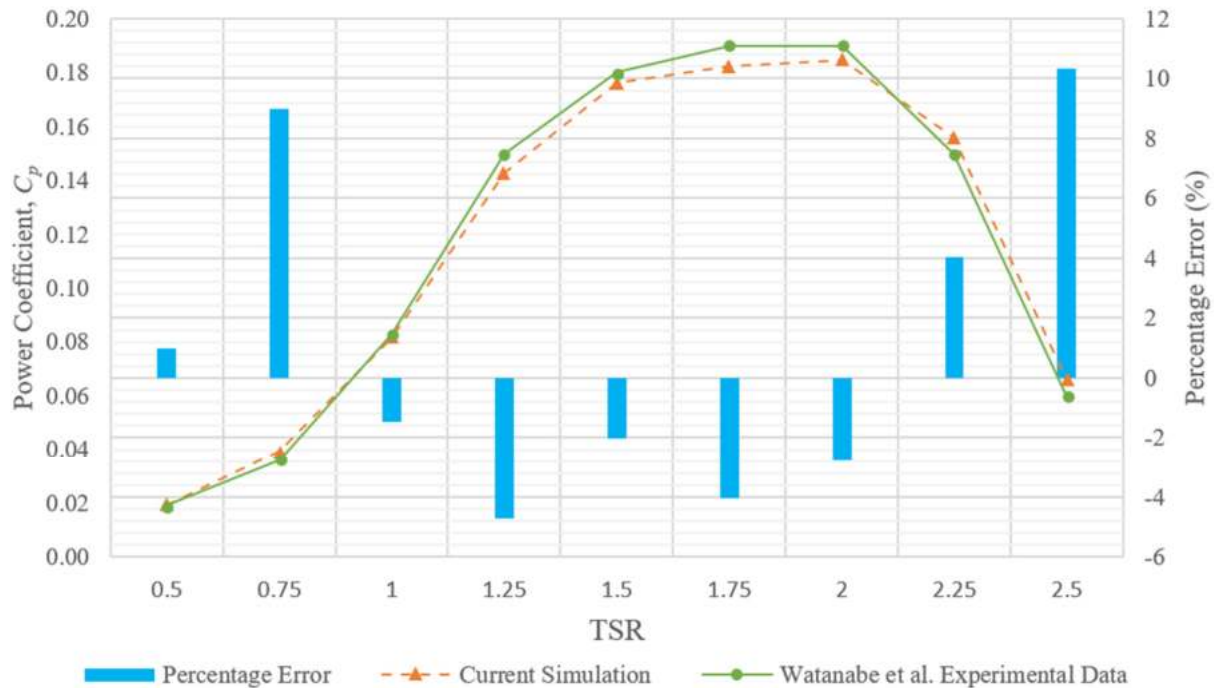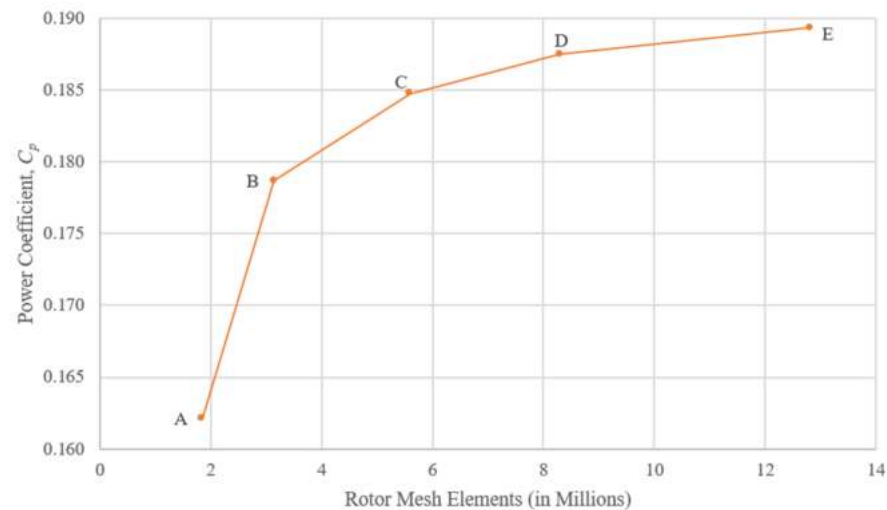

Figure 5. Model validation with experimental data from Watanabe et al. [25].

After establishing an appropriate VAWT model, opting for a fine and dense mesh is desirable to capture more details. However, this demands greater computational power, longer simulation time as well as more storage space. Therefore, a mesh independence test is carried out to obtain a mesh domain that can achieve a balance between accuracy and computational cost. In the mesh independence test, the cell size on the blades is manipulated to observe the effect on the blade torque coefficient while the tunnel mesh remains unchanged. Five meshes with cell sizes of 5, 3, 2, 1.5 and 1.2 mm are generated, corresponding to Meshes A, B, C, D, and E, respectively, as shown in Table 2. Note that in the model validation, the cell size on the blade is set as 2 mm. The detail of each mesh, together with the cycle-averaged power coefficient ($C_{P,ave}$) and the computational time required to complete a revolution, is tabulated in Table 2. The test is carried out at TSR 2, which is the maximum C_P from the experimental data, and a PC equipped with an AMD Ryzen Threadripper 3960X 24-core processor and 64 GB RAM is utilised to run all the simulations.

Figure 6 shows that as the blade element size is refined from 5 to 1.2 mm, the number of cells in the rotor mesh increases from 1.85 to 12.8 million cells. Mesh A shows the largest discrepancy, with a 10% error, while the C_P results converge closer to the experimental data as the number of elements increases. The C_P prediction from the finest mesh, Mesh E, is the closest to the experimental data, with only a 0.35% difference. However, the increase in accuracy is accompanied by a significantly longer computational time. Mesh D managed to return satisfactory results, with a much shorter computational time, with the discrepancy between Meshes D and E being only 0.95%. Therefore, the blade element size of 1.5 mm will be applied to all VAWT configurations investigated in this study.

Table 2. Detail of meshes.

Mesh	Blade Mesh Size (mm)	Rotor Mesh Elements (Million)	Computational Time Per Cycle (hrs)	$C_{P,ave}$	Percentage Error with Consecutive Cycle (%)
A	5.0	1.85	6	0.1622	9.23
B	3.0	3.14	8	0.1787	3.30
C	2.0	5.60	10	0.1848	1.44
D	1.5	8.30	12	0.1875	0.95
E	1.2	12.80	19	0.1893	-

Figure 6. Cycle-averaged C_P at TSR 2 for different blade mesh sizes.

3. Results and Discussions

3.1. Overall C_P Performance

The overall C_P performance is a prime indicator of the efficiency of a wind turbine in extracting wind energy. Therefore, the effectiveness of each endplate geometry can be reflected by comparing its overall C_P performance with the baseline turbine. Table 3 presents the cycle-averaged C_P attained from the CFD simulation for TSRs 1 and 2 for all VAWT configurations. Although the offset endplate had a similar configuration as in [18], it failed to replicate the positive results attained from the literature. Note that supporting struts, which are placed at $4c$ from the top end, are included in [18], while they are absent in the current case. In their study, a 4.25% power enhancement is observed at TSR 3. For TSR 2, the performance difference between their endplate and baseline configurations is negligible, but the supporting strut is relocated to the top end of the blade with the endplate in this case. In the current study, the overall $C_{P,ave}$ showed −22.24% and −0.64% degradation compared to the baseline turbine at TSRs 1 and 2, respectively. Even though direct comparisons cannot be made, the deviation in results may be attributed to the smaller aspect ratio and turbine size adopted in the current simulation. The deterioration of $C_{P,ave}$ is also observed in [12] below TSR 2 for a flat offset endplate with a smaller $0.18c$ offset. Other endplate geometries managed to elevate the overall $C_{P,ave}$ over the baseline turbine in both TSRs, albeit the underwhelming improvement being less than 2%. The marginal performance improvement is due to the endplate mainly improving the flow of a small section near the blade tip, while most of the torque is driven by the remaining blade span. The asymmetric and symmetric V endplates have the best performance in TSRs 1 and 2, respectively.

Table 3. Cycle-averaged C_P performance at TSRs 1 and 2.

VAWT Configuration	TSR 1		TSR 2	
	$C_{P,ave}$	Percentage Improvement (%)	$C_{P,ave}$	Percentage Improvement (%)
Baseline	0.0805	-	0.1875	-
Offset	0.0626	-22.24	0.1863	-0.64
Symmetric V	0.0815	1.31	0.1908	1.73
Asymmetric	0.0820	1.88	0.1902	1.42
Triangular	0.0807	0.27	0.1907	1.68

As shown in Figure 7, the contribution from two turbine blades leads to two C_P maxima and minima in one revolution for the total C_P of the VAWT. All endplate configurations managed to raise the maxima compared to the baseline turbine in both TSRs, and this suggests that the reduction of tip loss effect takes place in this region. The offset endplate showed the highest maxima, while the performance gap between the asymmetric, symmetric V, and triangular endplates is negligible. In TSR 1, the offset endplate showed a sharp decrease in C_P beyond the maxima (i.e., $90° < \theta < 120°$ and $270° < \theta < 330°$), as shown in Figure 7a. Meanwhile, the remaining three endplate configurations closely followed the baseline turbine, with a slightly lower C_P. From Figure 7b, the offset endplate lowers the minima, but the remaining three endplate configurations perform similarly to the baseline turbine. Besides that, all endplate configurations return slightly lower C_P when the blades move toward the upwind direction (i.e., $20° < \theta < 60°$ and $190° < \theta < 240°$) in TSR 2. The C_P reduction in this region is more significant for the offset endplate, while the symmetric V endplate performs more closely to the baseline turbine. It is also observed that the maxima shifts from 70° to 100° when the TSR increases from 1 to 2.

To investigate the performance differences between each endplate configuration and the baseline turbine, a vorticity diagram is plotted, as illustrated in Figure 8, with the vorticity level set at 0.0005. The azimuthal angle of Blade 1 is set as $\theta = 60°$ and $\theta = 90°$ for TSRs 1 and 2, respectively, as it corresponds to the location right before Blade 1 reaches the peak of C_P maxima, as presented in Figure 7. Overall, the vorticity curl is higher at TSR 2 than at TSR 1 across the board. In TSR 1, vortex shedding is observed in all VAWT configurations. The baseline turbine leaves a long trailing vortex behind both ends of Blade 1; however, the vortex is shredded into smaller structures in all endplate configurations. The vortex structure between the blades is the largest with the offset endplate. Hence, the interaction of the blade with the large vortex structure, as shown in Figure 9, may explain the sharp power degradation at around $\theta = 90°$. In TSR 2, a trailing vortex is present in all VAWT configurations, and the offset endplate once again has the largest vortex structure. A pair of trailing vortex structures is also present at both ends of the turbine, unlike in TSR 1, where it travels closer to the blade centre.

3.2. Blade 1 Performance

In this section, analysis is done on Blade 1 to understand the VAWT behaviour in the presence of different endplate geometries. From Figure 10, the trend is similar to the results found in the overall C_P in both TSRs. The offset endplate attains the highest maxima and is followed by the asymmetric, symmetric V, and triangular endplates, which perform similarly to one another. In the downwind region, the performance of all endplate configurations is slightly inferior compared to the baseline turbine in both TSRs, especially the offset endplate. At TSR 1, although the offset endplate outperforms at maxima ($\theta = 70°$), the sharp drop of C_P at $80° < \theta < 140°$ results in the total performance being worse than the baseline. This is because a greater suction pressure loss happens on the offset endplate; this is probably caused by the wide endplate region on the leading edge. As shown in Figure 11, the baseline and the symmetric V endplates possess similar pressure distributions at the suction side of the blade near the trailing edge. However, the pressure loss is higher along

the trailing edge of the offset endplates, which leads to a lower pressure difference between the blade surfaces and causes a sudden drop in the C_P.
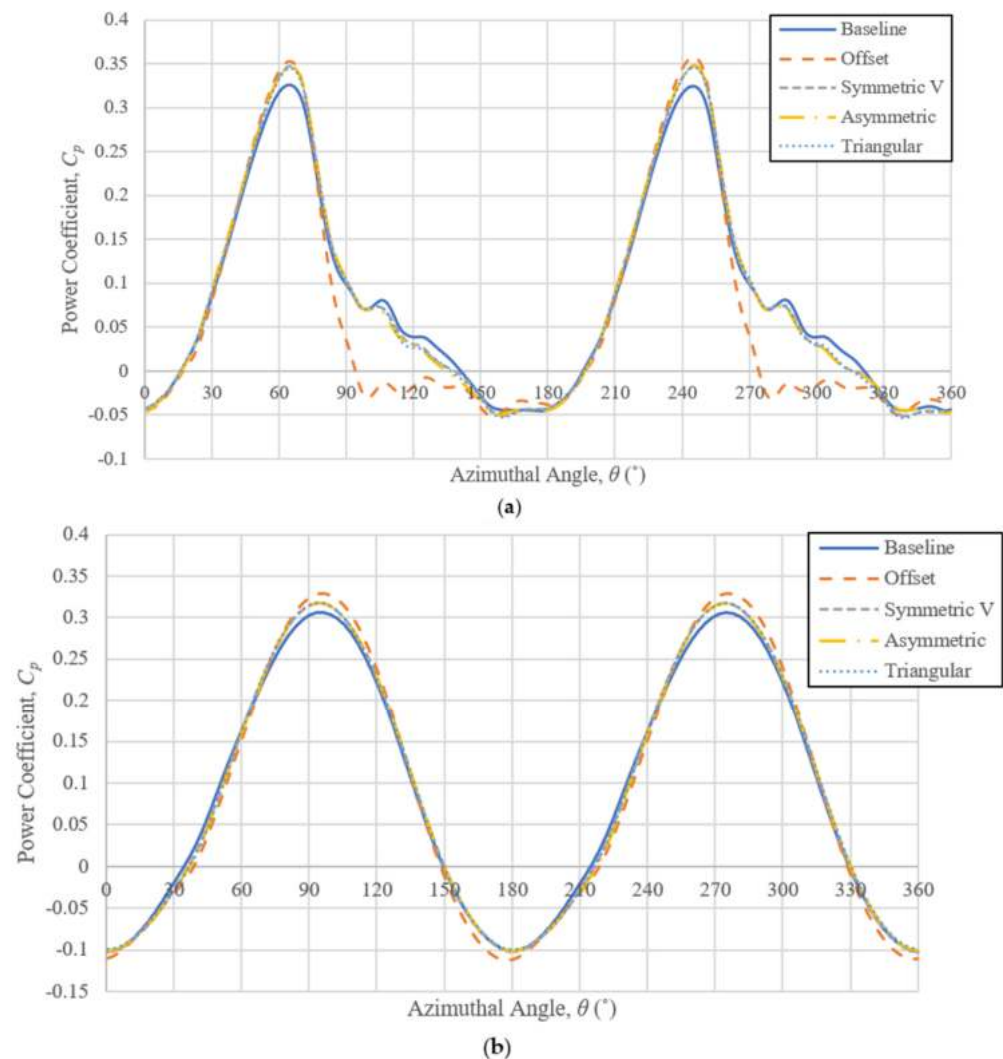

Figure 7. Overall C_P vs. azimuthal angle at (**a**) TSR 1 and (**b**) TSR 2.

As the C_P performance varies with the distance from the blade tip [18], the surface of Blade 1 is sectioned at different blade heights to observe the variation of C_P against blade height. From Table 4, the presence of an endplate greatly improves the power coefficient at the blade tip region in both TSRs 1 and 2. The cycle-averaged C_P increases significantly, beyond 1410%, in TSR 1 compared to the baseline turbine at 0.015625H. In TSR 2, the asymmetric, triangular, and, especially, offset endplates invert the negative C_P to a positive value. Although the symmetric V endplate shows a slight negative C_P at the blade tip, nevertheless, it is still an improvement compared with the baseline turbine. These results indicate that endplates are very effective at minimising the tip loss effect at the blade tip region.

From Figure 12, the C_P enhancement at the blade tip region is mainly contributed by the higher maxima achieved in the upwind region compared to the baseline turbine. In both TSRs, the offset endplate attains the highest maxima and is followed by the asymmetric, triangular, and symmetric endplates. Although the baseline turbine underperforms in the upwind region, especially in TSR 2, its performance in the downwind region is slightly better than the endplate configurations. Compared to TSR 1, the performance gap between the offset endplate and other endplate configurations in TSR 2 is much more significant. A second smaller local maxima is observed in Figure 12b, where the offset endplate returns

a higher C_P than other endplate configurations. It is also observed that the peak of C_P takes place at different azimuthal angles, depending on the endplate geometry in TSR 1. The offset endplate reaches its peak at $\theta = 70°$ and is followed by the other three endplates at $\theta = 100°$ and the baseline at $\theta = 110°$.
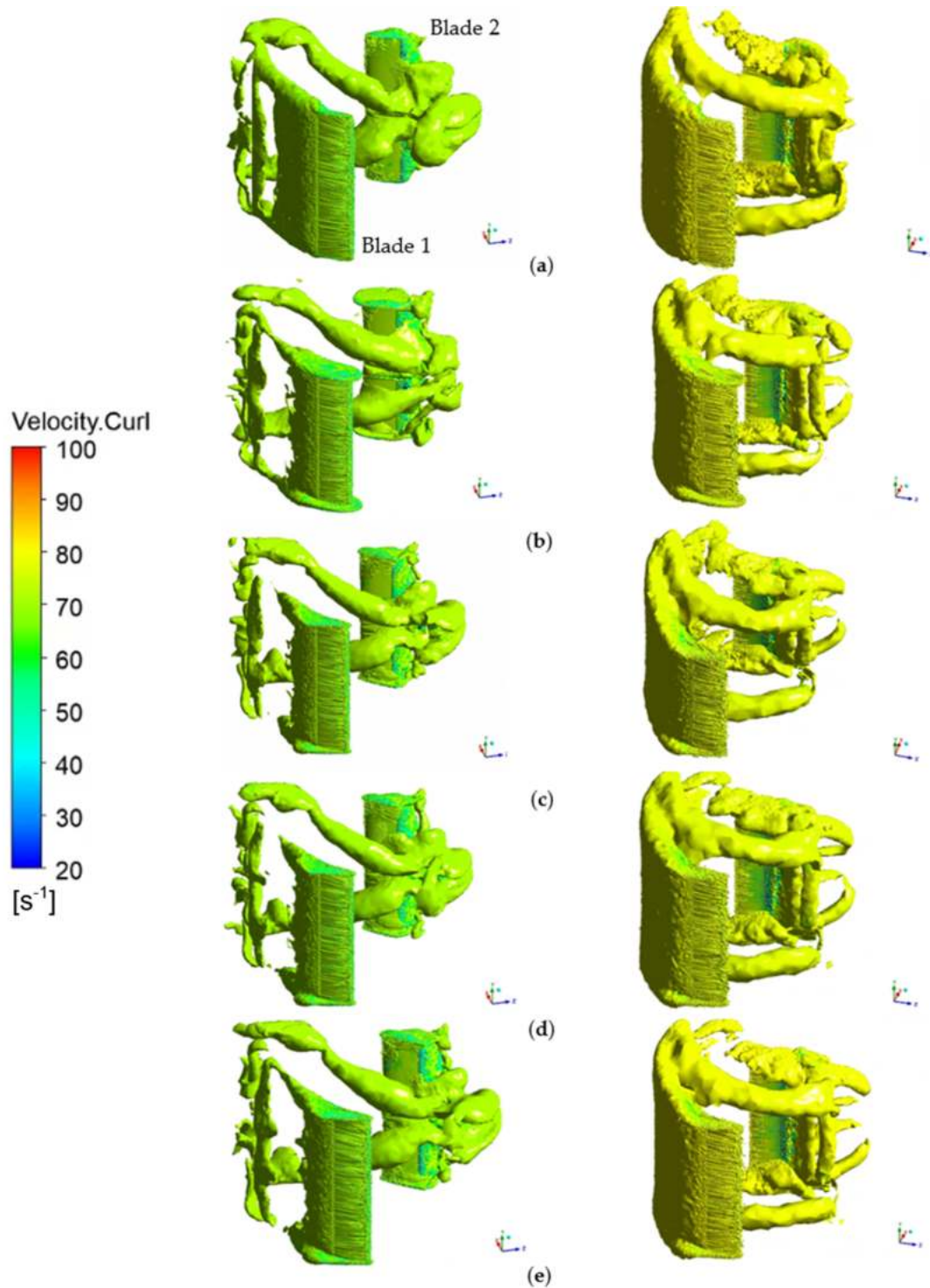

Figure 8. Vorticity of (**a**) baseline, (**b**) offset, (**c**) symmetric V, (**d**) asymmetric, and (**e**) triangular endplates at $\theta = 60°$ in TSR 1 (left column) and $\theta = 90°$ in TSR 2 (right column).
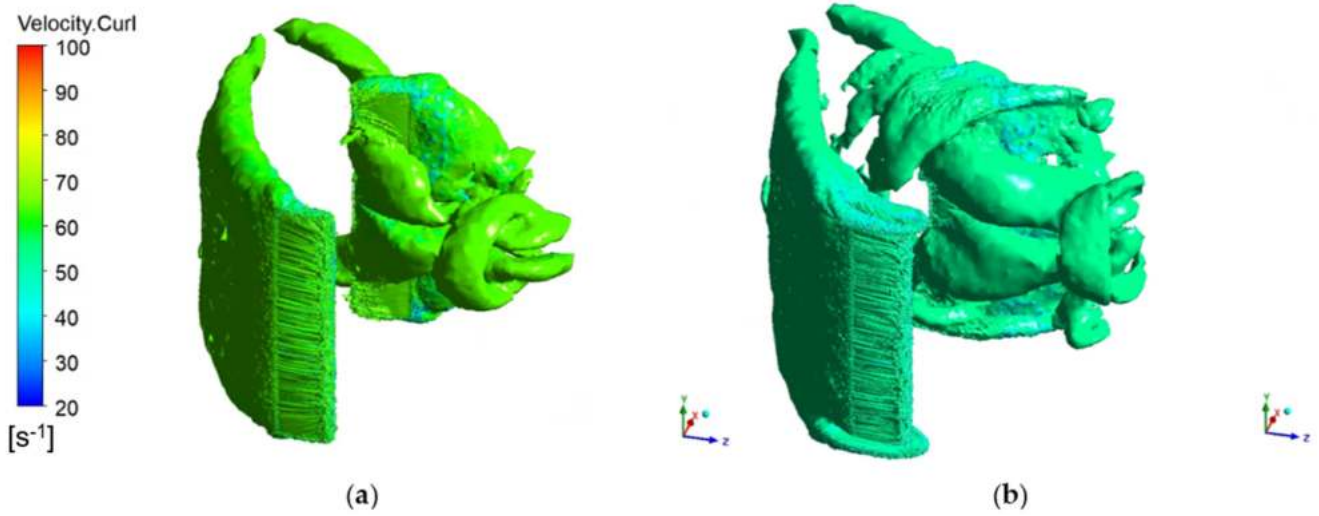
Figure 9. Vorticity of (**a**) baseline; (**b**) offset endplate at $\theta = 90°$ in TSR 1.
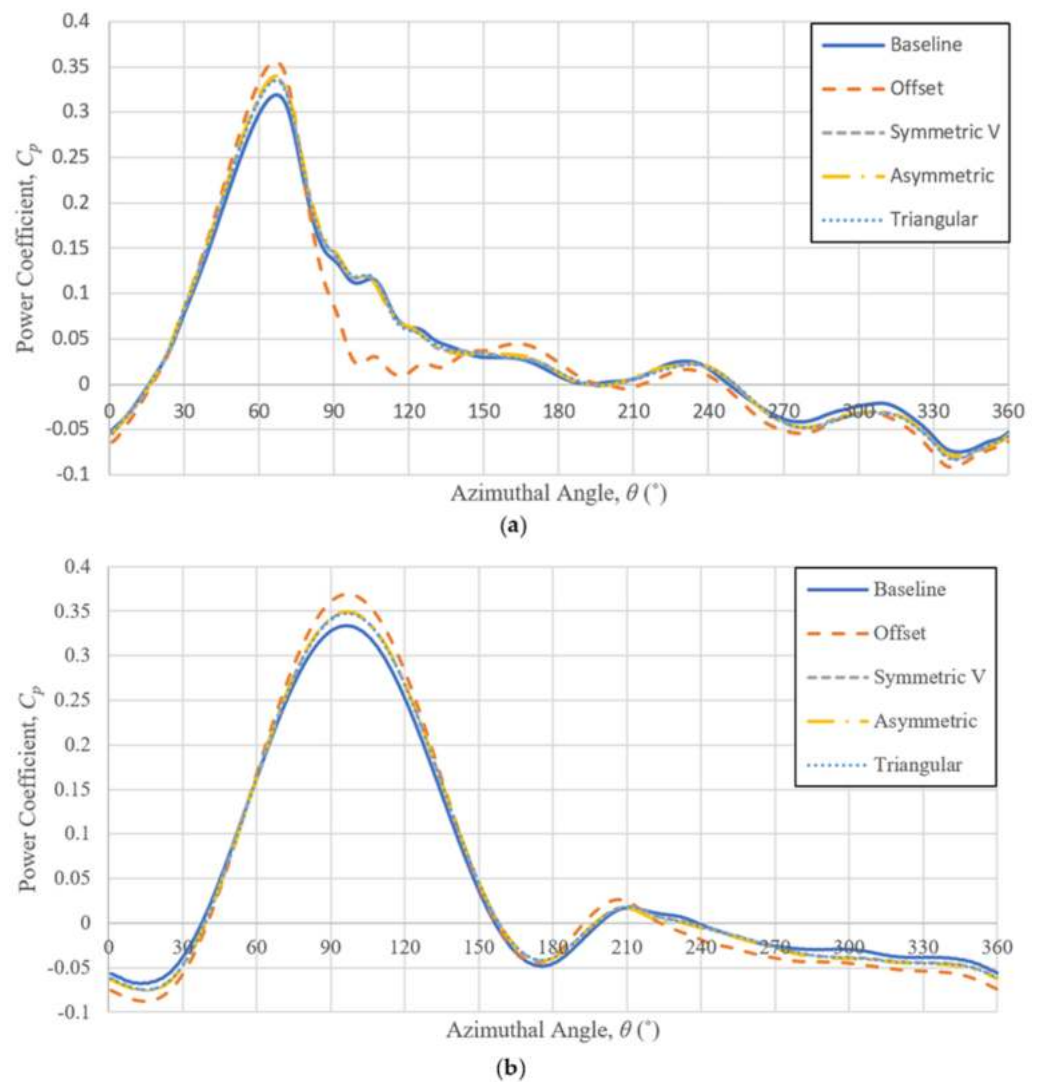
Figure 10. Blade 1 C_P vs. azimuthal angle at (**a**) TSR 1 and (**b**) TSR 2.
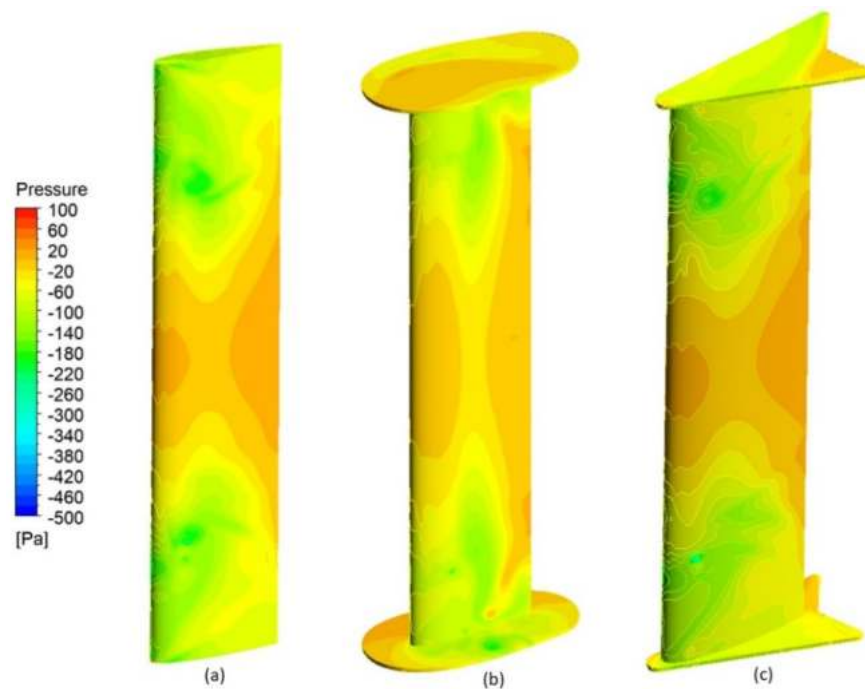
Figure 11. Pressure distribution on the suction surface of (**a**) baseline; (**b**) offset; (**c**) symmetry V endplate at $\theta = 120°$.

Table 4. Cycle-averaged C_P at 0.015625H in TSRs 1 and 2.

VAWT Configuration	TSR 1		TSR 2	
	$C_{P,ave}$	Percentage Improvement (%)	$C_{P,ave}$	Percentage Improvement (%)
Baseline	0.0020	-	−0.1409	-
Offset	0.0304	1410.53	0.0897	163.68
Symmetric V	0.0331	1542.47	−0.0027	98.10
Asymmetric	0.0331	1542.64	0.0036	102.54
Triangular	0.0353	1650.82	0.0077	105.50
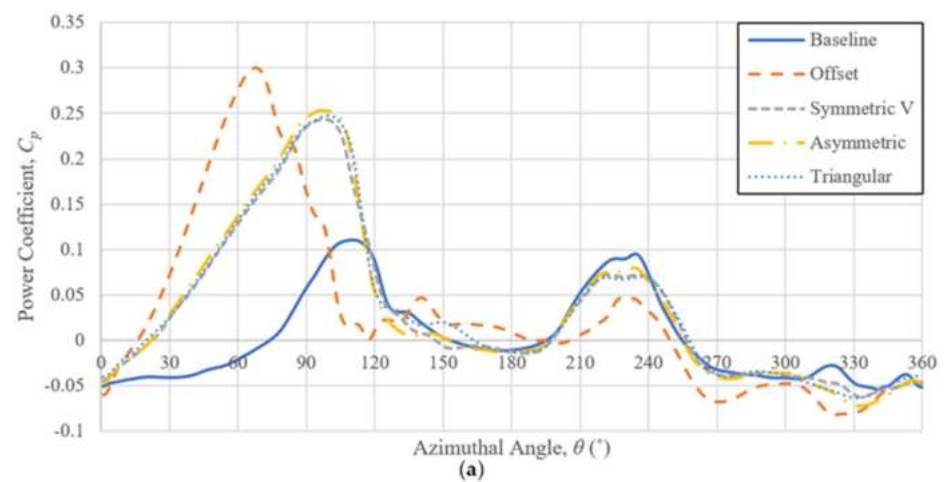
Figure 12. *Cont.*
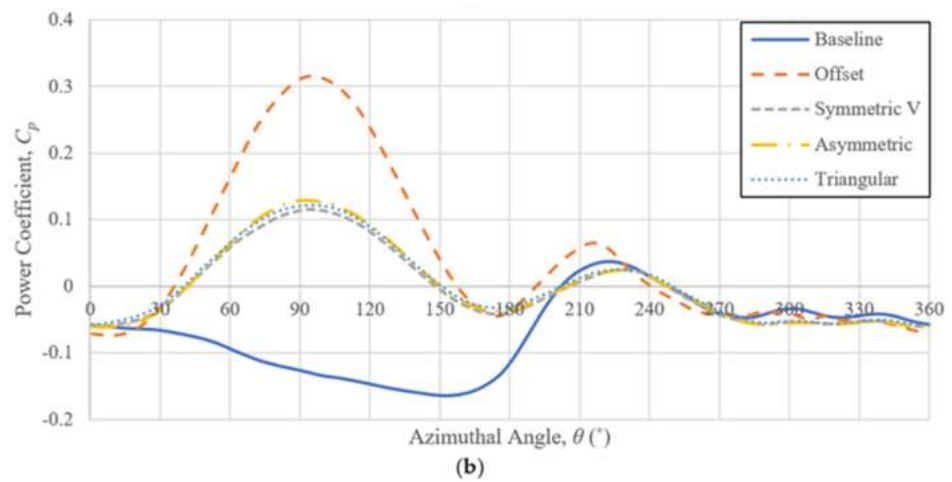
Figure 12. Comparison of C_P at 0.015625H of Blade 1 in (**a**) TSR 1 and (**b**) TSR 2.

Beyond the blade tip, the C_P difference is expected to decrease towards the mid-blade span for all endplate configurations; similar results are presented in [18,33]. This is because the tip loss effect is not significant at the blade centre. However, the results in TSR 1 start to deviate from the previous literature [18,33] beyond 0.125H. As illustrated in Figure 13a, the C_P at 0.25H to 0.5H drops below the level from 0.03125H to 0.125H. Dynamic stall at the low TSR might give rise to a dispute of the results. Besides that, all endplate configurations fail to improve their performance at 0.25H. Although the offset endplate shows inferior performance from 0.0625H to 0.25H, it manages to overcome other configurations at 0.5H.
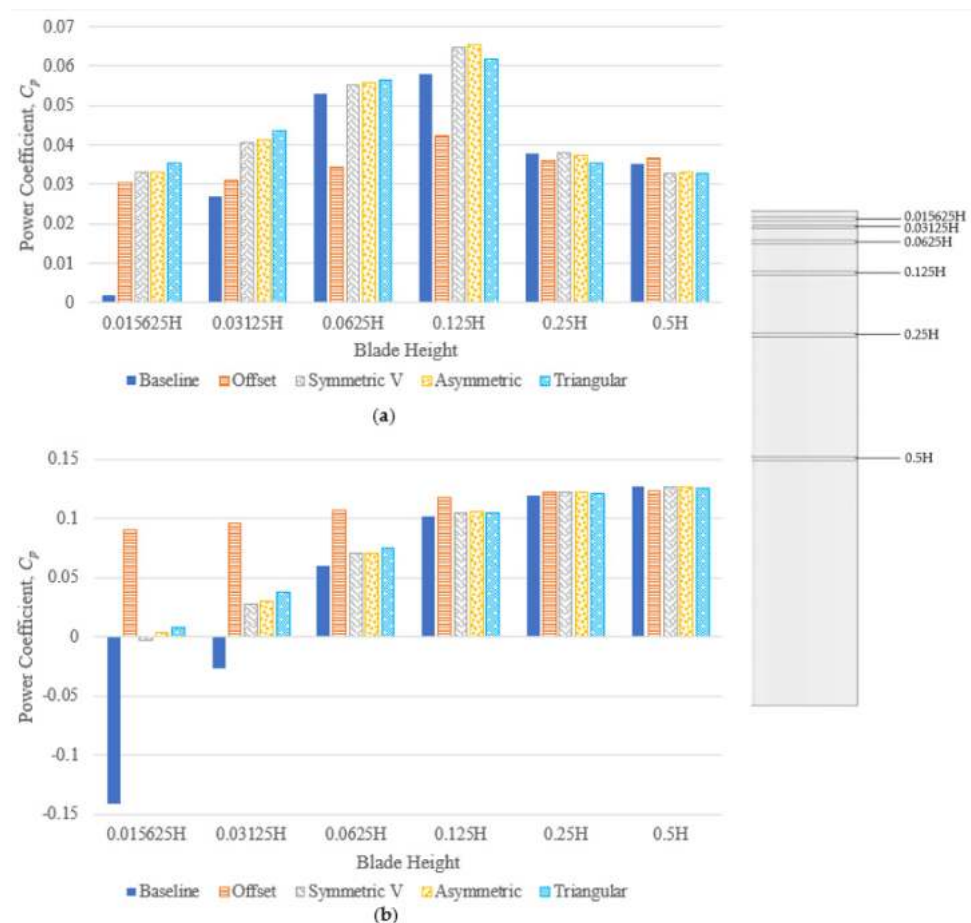

Figure 13. Breakdown of C_P contribution on Blade 1 at different blade heights in (**a**) TSR 1 and (**b**) TSR 2.

The results from TSR 2, presented in Figure 13b, agree well with the previous literature [18,33]. The offset endplate effectively enhances blade performance, especially at the blade tip region. Concurrently, the remaining three endplate configurations show smaller performance improvements before they overcome the offset endplate beyond 0.25*H*.

To gain further insight into the results, the pressure contour on Blade 1's surface is extracted on $\theta = 60°$ and $\theta = 90°$ for TSRs 1 and 2, respectively, as illustrated in Figures 14 and 15. This corresponds to the location right before Blade 1 reaches the peak of C_P maxima at TSRs 1 and 2. At the blade tip region, the pressure distribution on the baseline turbine is uneven on both sides of Blade 1. The loss of pressure on the pressure side leads to a degraded C_P output near the blade tips. The uniformity of pressure distribution is improved with the presence of the endplate in both TSRs. Notably, the offset endplate offers better uniformisation at the region around the leading edge than all other configurations. This is due to the offset endplate having a larger area allocated around the leading edge in contrast with other endplate configurations that have a pointed design that covers a much smaller area. Thus, the offset endplate is more effective in blocking the spanwise flow, as indicated by the uniform pressure contour around the blade tip region. The pressure distribution around the trailing edge is also enhanced over the baseline turbine, and the results are similar among all endplate configurations.
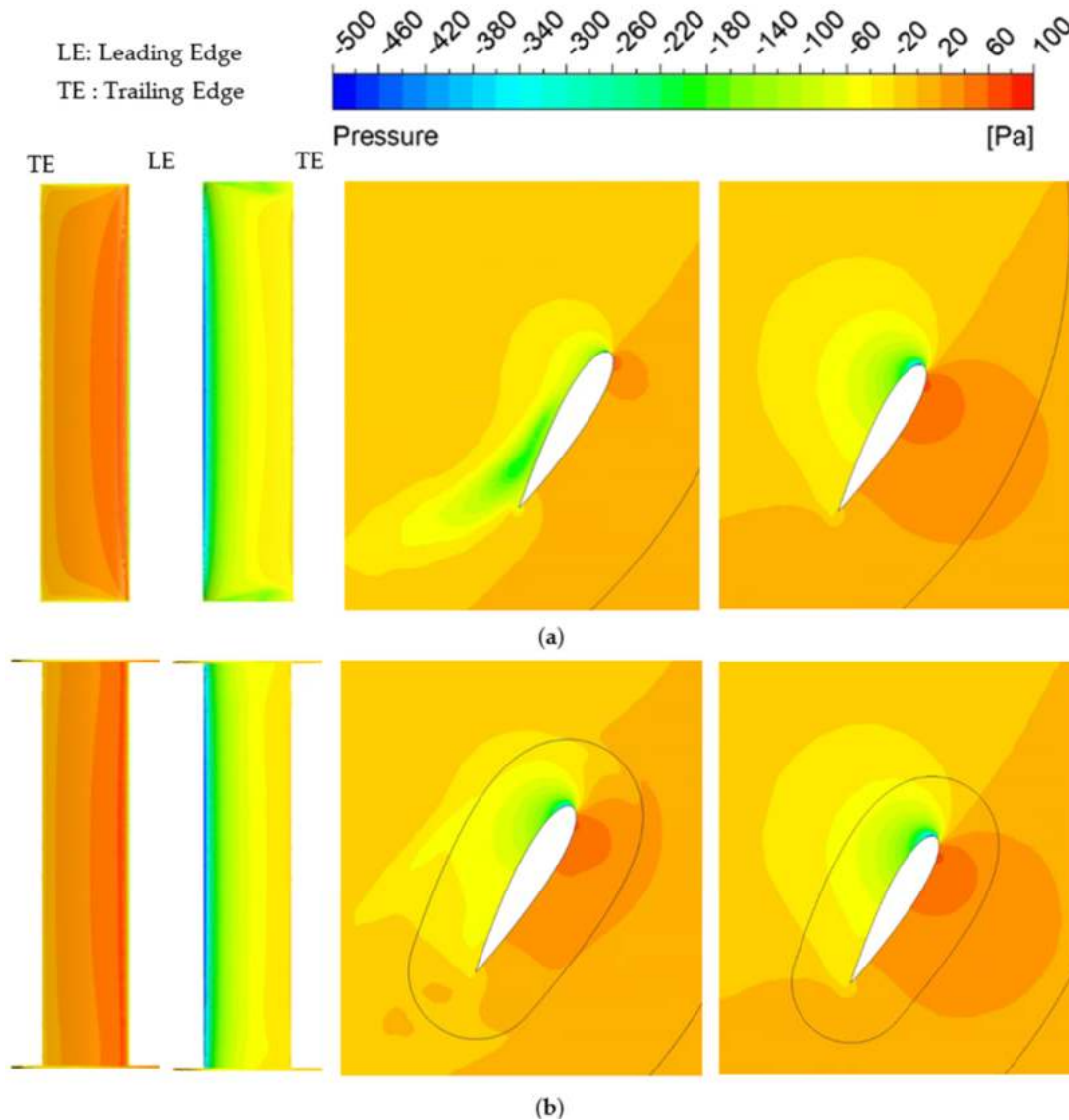

Figure 14. *Cont.*
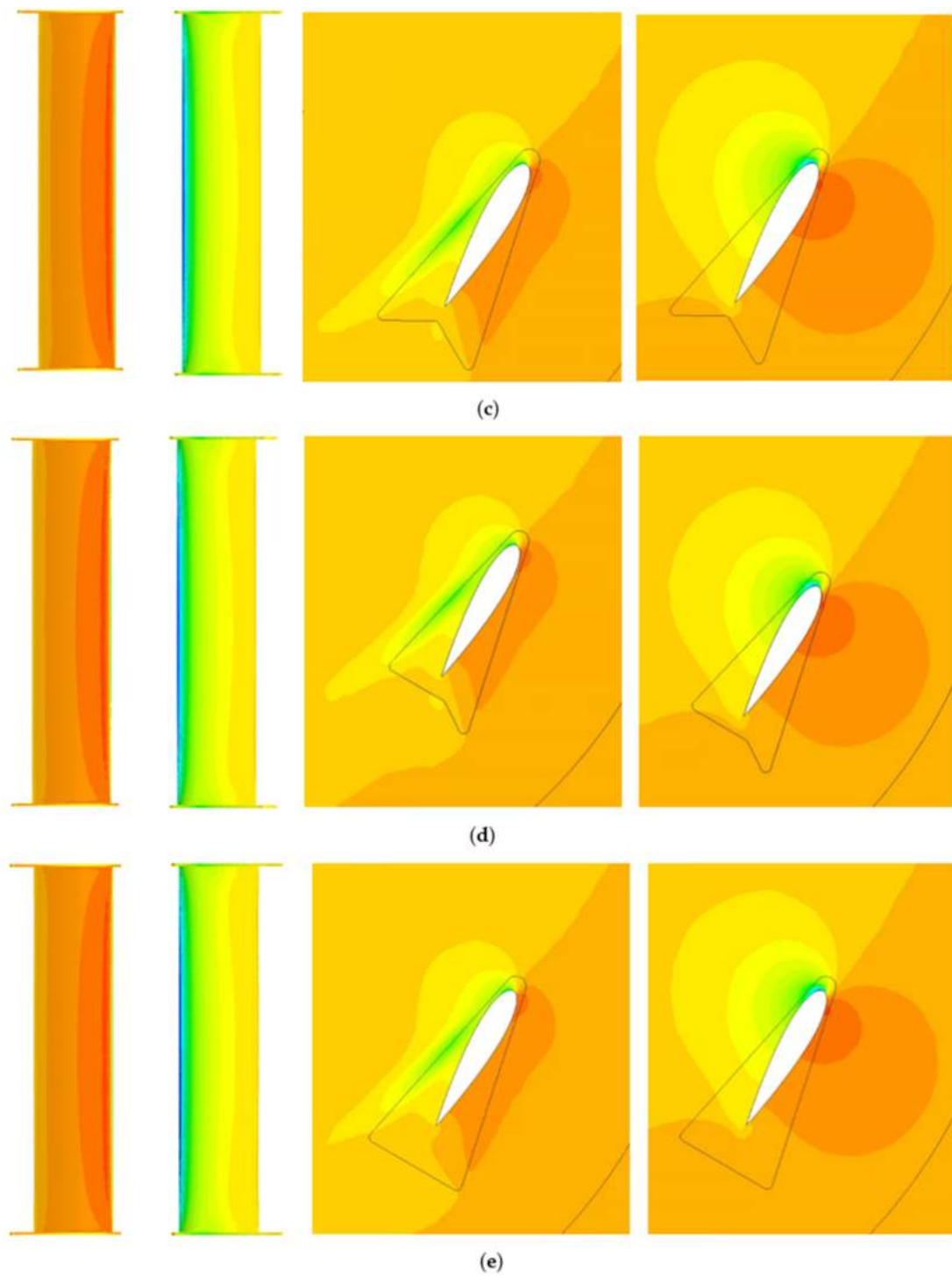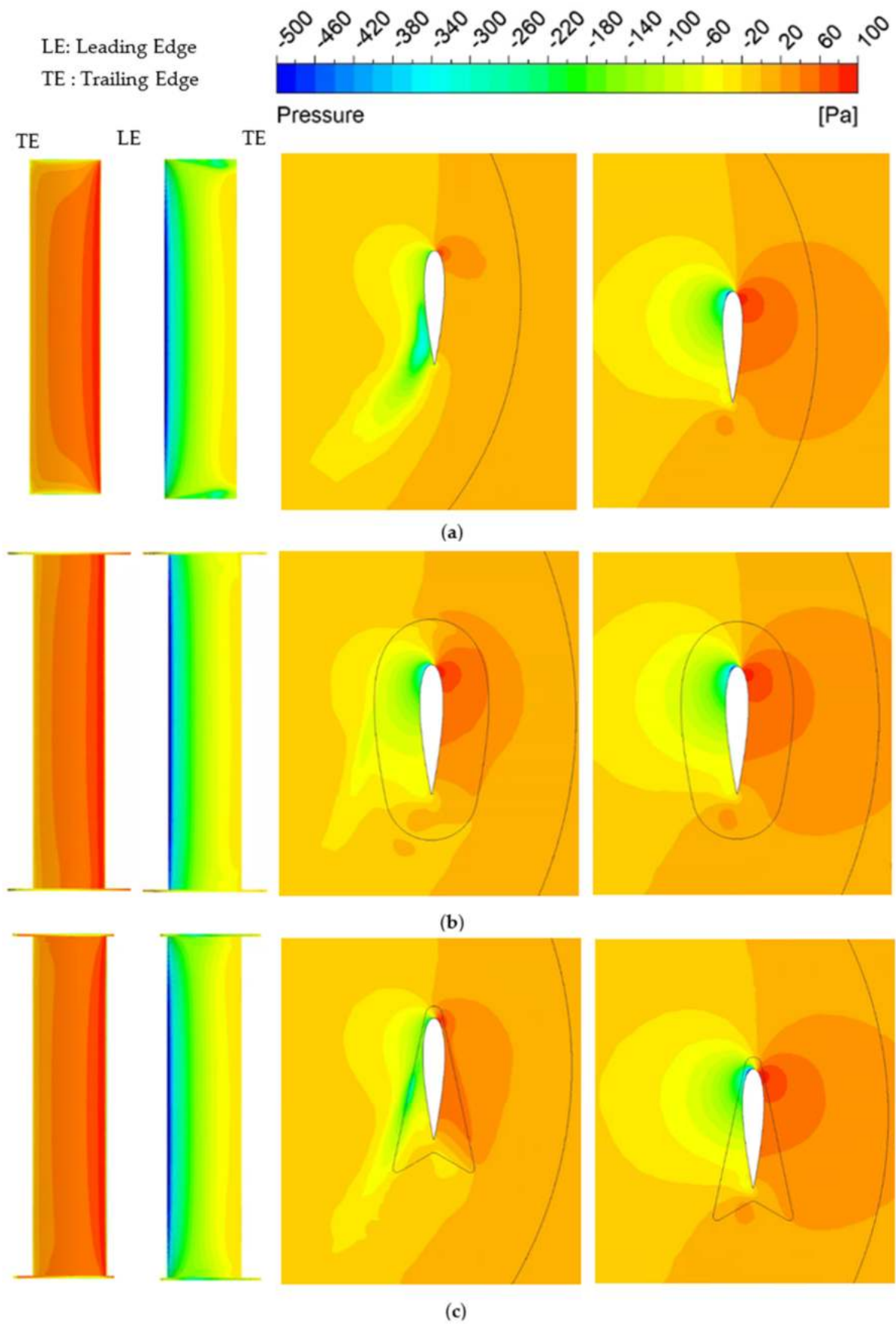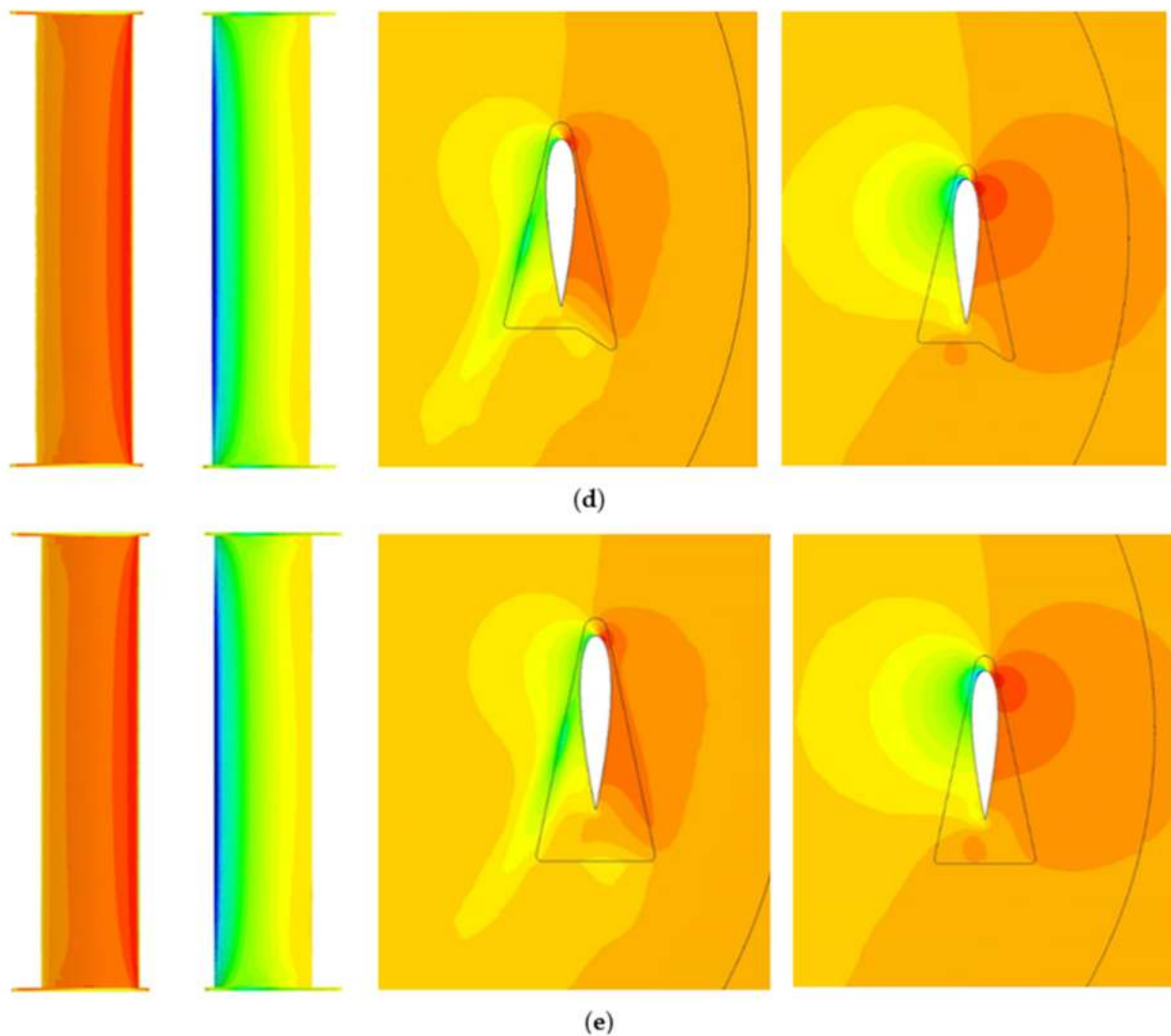
Figure 14. From left to right is the pressure distribution at the pressure side, suction side, at 0.015625H and 0.5H of Blade 1 at $\theta = 60°$ and TSR 1 for (**a**) baseline, (**b**) offset, (**c**) symmetric V, (**d**) asymmetric and (**e**) triangular endplates.

Figure 15. *Cont.*

Figure 15. From left to right is the pressure distribution at the pressure side, suction side, at 0.015625*H* and 0.5*H* of Blade 1 at $\theta = 90°$ and TSR 2 for (**a**) baseline, (**b**) offset, (**c**) symmetric V, (**d**) asymmetric and (**e**) triangular endplates.

A cut made on 0.015625*H* revealed a low-pressure region that spans across the chord length of the baseline turbine blade on the suction side in both TSRs. A similar observation is found in symmetric V, asymmetric, and triangular endplate configurations, with the exception of the low-pressure region detaching from the blade surface, unlike the baseline turbine. Such extension of the low-pressure region is absent in the offset endplate. On the pressure side, all endplates extended the high-pressure region towards the trailing edge. This increases the pressure difference between the pressure and suction sides at the blade tip and ultimately improves the C_P in that region. Besides that, different endplates also result in a slight pressure variation at the region behind the trailing edge. At 0.5*H* or the blade centre, the presence of the endplate shows a minimal difference.

3.3. Endplate Performance

A velocity streamline is plotted in Figure 16 for Blade 1 at $\theta = 60°$ and $\theta = 90°$ for TSRs 1 and 2, respectively, to visualise the flow around the blade tip. After the wind passes through the blade, the streamlines become uneven and spread wider, especially at TSR 2. The turbine performance will be adversely affected when the blade encounters unsteady wind in the downwind region. A swirling vortex is generated at the tip of the baseline turbine for both

TSRs, but this phenomenon is suppressed with the implementation of endplates. For TSR 2, the flow is also being deflected slightly upwards after passing Blade 1.
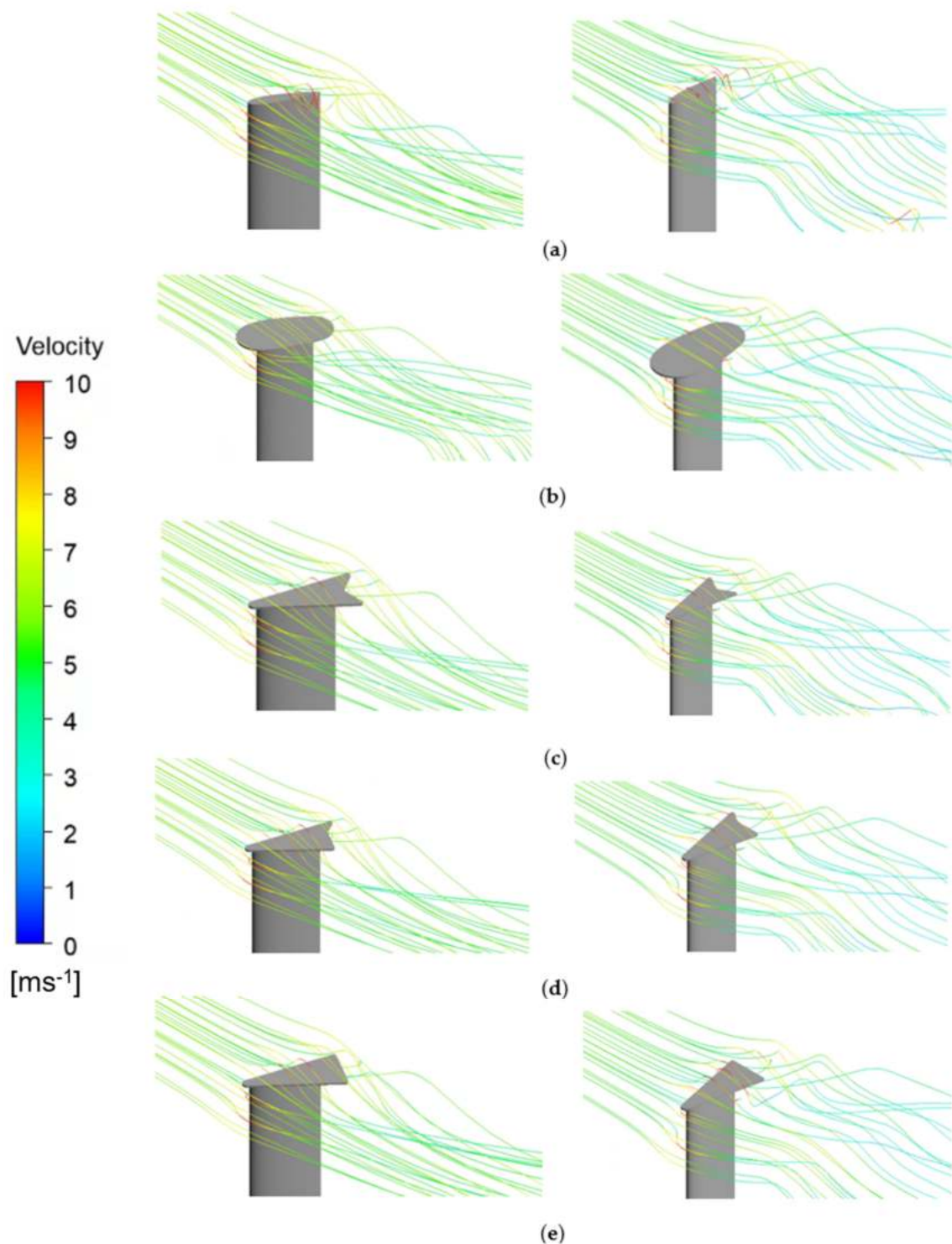

Figure 16. Velocity streamlines across the (**a**) baseline, (**b**) offset, (**c**) symmetric V, (**d**) asymmetric and (**e**) triangular endplates of Blade 1 at $\theta = 60°$ in TSR 1 (left column) and $\theta = 90°$ in TSR 2 (right column).

Although the implementation of endplates is bound to improve the overall performance of a VAWT [16], the additional surface area from the endplates will introduce more drag [9]. Figure 17a,b illustrate the C_P variation of the endplate throughout one revolution in TSRs 1 and 2, respectively. To the best of the authors' knowledge, such results have

not been reported in the previous literature. In both cases, the offset endplate encounters the largest C_P reduction. This can be correlated with its surface area, which is at least two times greater than the remaining endplate configurations. However, the C_P penalty is significantly reduced at around $\theta = 190°$. At TSR 1, the offset experiences the largest C_P reduction at $\theta = 345°$, while the rest takes place at $\theta = 30°$. As for TSR 2, the largest drag occurs at $30°$ for all endplate configurations, while minimum drag is observed at $200° < \theta < 240°$. The symmetric V, asymmetric, and triangular endplates perform similarly at TSR 2; however, the symmetric V endplate performs slightly better throughout most of the cycle. A larger discrepancy is observed in TSR 1, and these endplate configurations manage to return a positive C_P at $110° < \theta < 260°$.
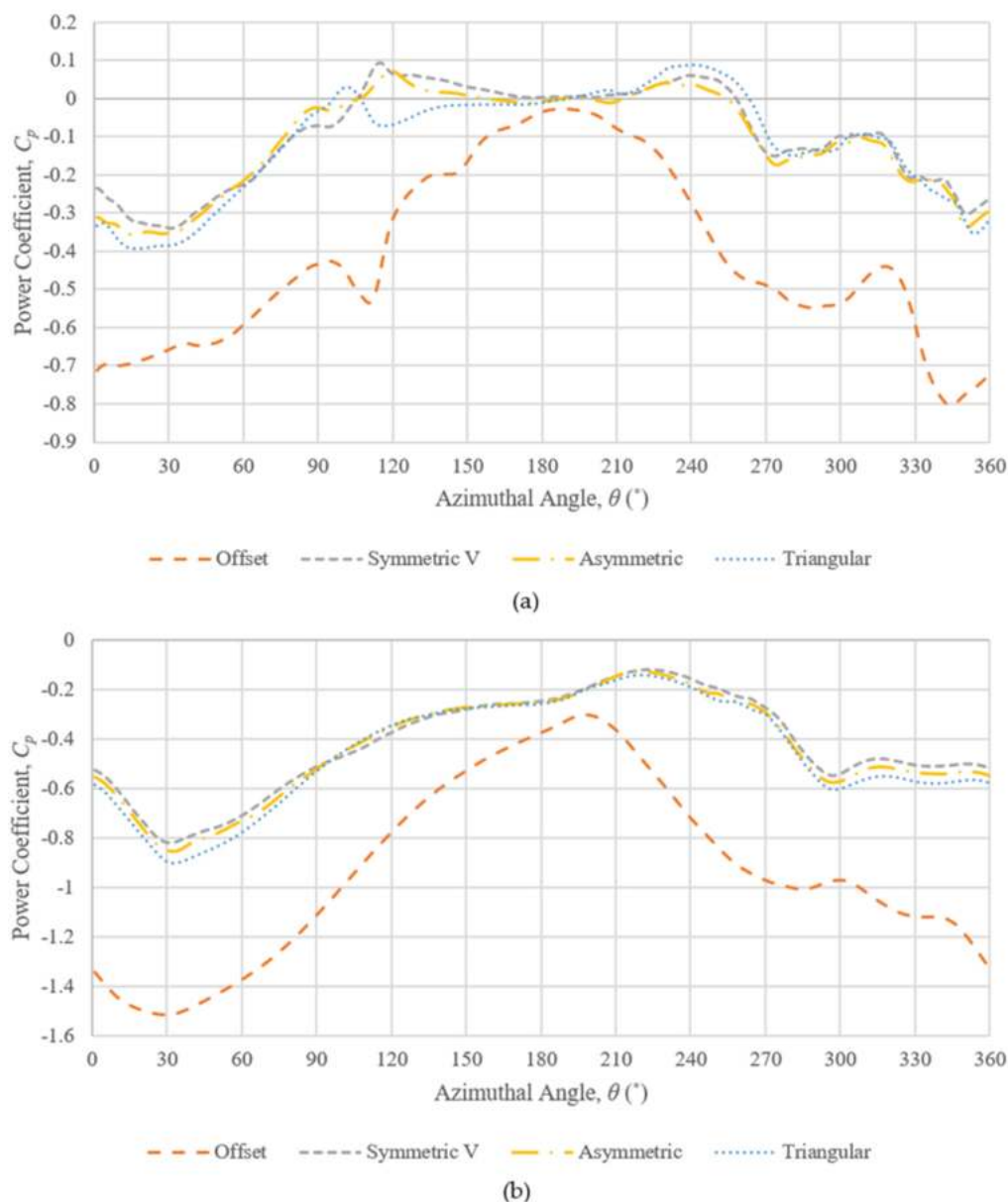

(a)

(b)

Figure 17. C_P on the endplate surface vs. azimuthal angle at (**a**) TSR 1 and (**b**) TSR 2.

The gain of C_P on the blade itself due to the endplate must overcome the drag introduced in order to achieve overall improvement. Tables 5 and 6 tabulate and compare the $C_{P,ave}$ on the effective blade surface against the net $C_{P,ave}$ generated by Blade 1 overall. The percentage reduction indicates the percentage of $C_{P,ave}$ reduced due to losses from the endplate. At the same time, the percentage improvement and net percentage improvement

indicate the improvement over the baseline turbine in the effective blade surface and overall blade, respectively.

Table 5. Breakdown of Blade 1 C_P in TSR 1.

VAWT Configuration	$C_{P,ave}$ on Effective Blade Surface	Net Blade 1 $C_{P,ave}$	Percentage Reduction (%)	Improvement on Effective Blade Surface (%)	Net Percentage Improvement (%)
Baseline	0.0403	0.0403	0	-	-
Offset	0.0364	0.0311	14.56	−9.58	−22.74
Symmetric V	0.0421	0.0409	2.87	4.42	1.43
Asymmetric	0.0425	0.0411	3.22	5.38	1.98
Triangular	0.0415	0.0401	3.43	2.97	−0.56

Table 6. Breakdown of Blade 1 C_P in TSR 2.

VAWT Configuration	$C_{P,ave}$ on Effective Blade Surface	Net Blade 1 $C_{P,ave}$	Percentage Reduction (%)	Improvement on Effective Blade Surface (%)	Net Percentage Improvement (%)
Baseline	0.0939	0.0939	0	-	-
Offset	0.1164	0.0925	20.54	23.97	−1.49
Symmetric V	0.1062	0.0954	10.16	13.13	1.64
Asymmetric	0.1062	0.0950	10.54	13.13	1.21
Triangular	0.1066	0.0949	10.97	13.55	1.09

All endplate configurations on Blade 1 generated negative $C_{P,ave}$ in both TSRs, and the C_P compensated in TSR 2 is greater than TSR 1, as indicated by the larger percentage reduction across the board. Except for the offset endplate in TSR 1, all endplate configurations elevated the $C_{P,ave}$ generated on the effective blade surface. In TSR 1, the offset endplate experiences a 22.74% net performance reduction as it fails to return improvement on the blade in the first place. Although it manages to improve the blade performance by 23.97% in TSR 2, the large drag induces compensates for all the performance enhancement on the turbine blades and, ultimately, leads to a negative value being obtained, contributing to the low overall C_P output. Other endplates manage to maintain a 1.09% to 1.98% improvement after accounting for the endplate losses, except for the triangular endplate at TSR 1. The symmetric V endplate consistently has the lowest drag induced, and the enhancement it brings to the blade surface is in between the asymmetric and triangular endplates. Hence, the symmetric endplate is considered the best design among the four endplates as it performs the best at TSR 2, which is the optimum TSR for this VAWT.

4. Conclusions

In summary, the implementation of well-designed endplate geometry can have a positive effect on the C_P performance of a VAWT. From a CFD simulation, the symmetric V and asymmetric endplates are the best performers in TSRs 1 and 2, respectively, although the overall C_P enhancement is less than 2%. At the blade tip region, endplates can result in a performance boost of up to 163.68% and 1650.82% in TSRs 1 and 2, respectively. Besides that, the endplate effectively blocks the spanwise flow and improves pressure uniformisation near the blade tip. Thus, the loss of pressure difference across the pressure and suction sides of the blade can be minimised. The swirling vortex generated by the baseline turbine at the open-ended blade tip also can be suppressed with endplates. Endplates can effectively improve the C_P performance on the blade surface; however, the induced drag limits the net power improvement. Although the offset endplate offers the best performance enhancement on the blade surface in TSR 2, the large drag induced by the large surface area degrades the VAWT's overall performance. On the other hand, the induced drag from the symmetric V endplate is the lowest among the four endplates tested, and it performs the

best at the optimum TSR. Hence, it is considered the best overall design in the current study. Further investigation is still required to explore more endplate geometries as the current study has only focused on four different geometries. This study has only focused on the flow characteristics; other factors such as manufacturing complexity, material strength, and cost are not considered while implementing the endplate geometries for this CFD simulation. An endplate design that can achieve a balance between performance and cost is crucial for minimising the cost of energy (COE) of a VAWT. Therefore, this research contributes to the study of the optimisation of endplate parameters to further enhance the power generation capability of VAWTs.

References

1. GWEC. Global Wind Report 2022. Global Wind Energy Council. 2022. Available online: https://gwec.net/global-wind-report-2022/ (accessed on 10 July 2022).
2. Malla, A.; Han, Z.; Zhou, D. Effect of a winglet on the Power Augmentation of Straight Bladed Darrieus Wind Turbine. *IOP Conf. Ser. Earth Environ. Sci.* **2020**, *505*, 012041. [CrossRef]
3. Tjiu, W.; Marnoto, T.; Mat, S.; Ruslan, M.H.; Sopian, K. Darrieus vertical axis wind turbine for power generation II: Challenges in HAWT and the opportunity of multi-megawatt Darrieus VAWT development. *Renew. Energy* **2015**, *75*, 560–571. [CrossRef]
4. Laín, S.; Taborda, M.A.; López, O.D. Numerical Study of the Effect of Winglets on the Performance of a Straight Blade Darrieus Water Turbine. *Energies* **2018**, *11*, 297. [CrossRef]
5. Sharma, V.; Sharma, S.; Sharma, G. Recent development in the field of wind turbine. *Mater. Today Proc.* **2022**, *64*, 1512–1520. [CrossRef]
6. Arredondo-Galeana, A.; Brennan, F. Floating Offshore Vertical Axis Wind Turbines: Opportunities, Challenges and Way Forward. *Energies* **2021**, *14*, 8000. [CrossRef]
7. Dewan, A.; Gautam, A.; Goyal, R. Savonius wind turbines: A review of recent advances in design and performance enhancements. *Mater. Today Proc.* **2021**, *47*, 2976–2983. [CrossRef]
8. Lam, H.F.; Peng, H.Y. Study of wake characteristics of a vertical axis wind turbine by two- and three-dimensional computational fluid dynamics simulations. *Renew. Energy* **2016**, *90*, 386–398. [CrossRef]
9. Gosselin, R.; Dumas, G.; Boudreau, M. Parametric study of H-Darrieus vertical-axis turbines using CFD simulations. *J. Renew. Sustain. Energy* **2016**, *8*, 053301. [CrossRef]
10. Zhang, T.T.; Elsakka, M.; Huang, W.; Wang, Z.G.; Ingham, D.B.; Ma, L.; Pourkashanian, M. Winglet design for vertical axis wind turbines based on a design of experiment and CFD approach. *Energy Convers. Manag.* **2019**, *195*, 712–726. [CrossRef]
11. Howell, R.; Qin, N.; Edwards, J.; Durrani, N. Wind tunnel and numerical study of a small vertical axis wind turbine. *Renew. Energy* **2010**, *35*, 412–422. [CrossRef]
12. Miao, W.; Liu, Q.; Xu, Z.; Yue, M.; Li, C.; Zhang, W. A comprehensive analysis of blade tip for vertical axis wind turbine: Aerodynamics and the tip loss effect. *Energy Convers. Manag.* **2022**, *253*, 115140. [CrossRef]
13. Jung, J.H.; Kim, M.J.; Yoon, H.S.; Hung, P.A.; Chun, H.H.; Park, D.W. Endplate effect on aerodynamic characteristics of three-dimensional wings in close free surface proximity. *Int. J. Nav. Archit. Ocean. Eng.* **2012**, *4*, 477–487. [CrossRef]
14. Syawitri, T.P.; Yao, Y.; Yao, J.; Chandra, B. A review on the use of passive flow control devices as performance enhancement of lift-type vertical axis wind turbines. *Wiley Interdiscip. Rev. Energy Environ.* **2022**, *11*, e435. [CrossRef]
15. Johansen, J.; Sørensen, N. Numerical Analysis of Winglets on Wind Turbine Blades using CFD. In Proceedings of the in European Wind Energy Conference, Milan, Italy, 7–10 May 2007.

16. Amato, F.; Bedon, G.; Castelli, M.R.; Benini, E. Numerical Analysis of the Influence of Tip Devices on the Power Coefficient of a VAWT. *Int. J. Aerosp. Mech. Eng.* **2013**, *7*, 1053–1060.

17. Mousavi, M.; Masdari, M.; Tahani, M. Power performance enhancement of vertical axis wind turbines by a novel gurney flap design. *Aircr. Eng. Aerosp. Technol.* **2022**, *94*, 482–491. [CrossRef]

18. Jiang, Y.; He, C.; Zhao, P.; Sun, T. Investigation of Blade Tip Shape for Improving VAWT Performance. *J. Mar. Sci. Eng.* **2020**, *8*, 225. [CrossRef]

19. Premkumar, T.M.; Sivamani, S.; Kirthees, E.; Hariram, V.; Mohan, T. Data set on the experimental investigations of a helical Savonius style VAWT with and without end plates. *Data Brief* **2018**, *19*, 1925–1932. [CrossRef]

20. Kassab, S.Z.; Chemengich, S.J.; Lotfy, E.R. The effect of endplate addition on the performance of the savonius wind turbine: A 3-D study. *Proc. Inst. Mech. Eng. Part A J. Power Energy* **2022**, 09576509221098480. [CrossRef]

21. Daróczy, L.; Janiga, G.; Thévenin, D. Optimization of a winglet for improving the performance of an H-Darrieus turbine using CFD. In Proceedings of the 16th International Symposium on Transport Phenomena and Dynamics of Rotating Machinery, Honolulu, HI, USA, 10–15 April 2016.

22. Nathan, K.R.; Thanigaiarasu, S. Effect of different endplates on blade aerodynamic performance and blade loading of VAWT with symmetric airfoil blades. In Proceedings of the 2017 International Conference on Green Energy and Applications (ICGEA), Singapore, 25–27 March 2017; pp. 1–5. [CrossRef]

23. Mishra, N.; Gupta, A.S.; Dawar, J.; Kumar, A.; Mitra, S. Numerical and Experimental Study on Performance Enhancement of Darrieus Vertical Axis Wind Turbine With Wingtip Devices. *J. Energy Resour. Technol.* **2018**, *140*, 121201. [CrossRef]

24. Barnes, A.; Marshall-Cross, D.; Hughes, B.R. Towards a standard approach for future Vertical Axis Wind Turbine aerodynamics research and development. *Renew. Sustain. Energy Rev.* **2021**, *148*, 111221. [CrossRef]

25. Watanabe, K.; Takahashi, S.; Ohya, Y. Application of a Diffuser Structure to Vertical-Axis Wind Turbines. *Energies* **2016**, *9*, 406. [CrossRef]

26. Siddiqui, M.S.; Durrani, N.; Akhtar, I. Quantification of the effects of geometric approximations on the performance of a vertical axis wind turbine. *Renew. Energy* **2015**, *74*, 661–670. [CrossRef]

27. Aihara, A.; Mendoza, V.; Goude, A.; Bernhoff, H. Comparison of Three-Dimensional Numerical Methods for Modeling of Strut Effect on the Performance of a Vertical Axis Wind Turbine. *Energies* **2022**, *15*, 2361. [CrossRef]

28. ANSYS. *ANSYS Fluent—User Guide*, Release 17.2 ed; ANSYS Inc.: Canonsburg, PA, USA, 2016.

29. Menter, F.R. Two-equation eddy-viscosity turbulence models for engineering applications. *AIAA J.* **1994**, *32*, 1598–1605. [CrossRef]

30. Wong, K.H.; Chong, W.T.; Poh, S.C.; Shiah, Y.-C.; Sukiman, N.L.; Wang, C.-T. 3D CFD simulation and parametric study of a flat plate deflector for vertical axis wind turbine. *Renew. Energy* **2018**, *129*, 32–55. [CrossRef]

31. Dol, S.; Khamis, A.; Abdallftah, M.; Fares, M.; Pervaiz, S. CFD Analysis of Vertical Axis Wind Turbine with Winglets. *Renew. Energy Res. Appl.* **2022**, *3*, 51–59.

32. Maître, T.; Amet, E.; Pellone, C. Modeling of the flow in a Darrieus water turbine: Wall grid refinement analysis and comparison with experiments. *Renew. Energy* **2013**, *51*, 497–512. [CrossRef]

33. Yang, Y.; Guo, Z.; Zhang, Y.; Jinyama, H.; Li, Q. Numerical Investigation of the Tip Vortex of a Straight-Bladed Vertical Axis Wind Turbine with Double-Blades. *Energies* **2017**, *10*, 1721. [CrossRef]